Overturning in the Nordic Seas from 2002 to 2017 in the Arctic Subpolar gyre sTate Estimate

Birgit Klem Rønning Rinde

Supervisors: Kjetil Våge & Ailin Brakstad

Master Thesis in Physical Oceanography

Geophysical Institute

June 2022

UNIVERSITY OF BERGEN
Faculty of Mathematics and Natural Sciences

Abstract

A data-constrained, medium-resolution coupled sea ice-ocean state estimate, the Arctic Subpolar gyre sTate Estimate, is evaluated in the Nordic Seas. The state estimate is dynamically and kinematically consistent, and has a nominal resolution of $1/3°$, corresponding to 16 km in the Nordic Seas. It is biased low in density throughout the domain, most prominently in the Greenland and Iceland Seas where the water column above 1000 m is both too warm and too fresh. The deepest mixed layers are found in the West Spitsbergen Current instead of in the Greenland Sea. The overflow water spilling across the Greenland-Scotland Ridge is too light, and constitute a smaller volume than observations from the same period indicate. Other main features of the Nordic Seas are generally well reproduced. The state estimate is used to explore the overturning in the Nordic Seas, in particular to quantify the rate of dense-water production in each basin, and investigate the factors influencing the overturning. In the state estimate, the densest water of the Nordic Seas is formed in the Greenland Sea, and the near-surface salinity greatly influences its formation. The production rate of dense water is too low to realistically simulate the overflow across the Greenland-Scotland Ridge, a bias that contributes to a weakened Atlantic Meridional Overturning Circulation. In light of the expected increase in freshwater loading due to global warming, the Arctic Subpolar Gyre sTate Estimate may be more representative of the overturning in the Nordic Seas in a future warmer climate.

Contents

1 | **Introduction and background**

1.1 The Atlantic Meridional Overturning Circulation

Meridional oceanic transport of heat, freshwater, carbon, and nutrients is crucial to the world's climate (Bryden and Imawaki, 2011; Rhines et al., 2008). In the Atlantic Ocean, the poleward transport of heat is strongly connected to the Atlantic Meridional Overturning Circulation (AMOC; (Buckley and Marshall, 2016). The AMOC transports warm, saline water polewards from the equator in the upper kilometer of the water column. As the water proceeds northwards, it loses heat to the atmosphere, and thereby buoyancy. When returning to the south with increased density, it sinks into the abyss due to frictional forces from topography. It entrains ambient water and ventilates the deep ocean as North Atlantic Deep Water (NADW). To close the overturning cell, the NADW is lifted towards the surface by diapycnal mixing in the global ocean, and by wind-induced upwelling in the Southern Ocean (Marshall and Speer, 2012; Johnson et al., 2019). Today, most climate models predict a weakening of the AMOC due to global warming (Cheng et al., 2013). Global consequences on climate and marine ecosystems are expected following changes in the AMOC (Kuhlbrodt et al., 2007; Buckley and Marshall, 2016). Regarding the current state of the AMOC, results are contradictory; while the AMOC was in a state of reduced overturning between 2008 and 2018 at 26°N (Smeed et al., 2018), no such weakening has been observed in the Nordic Seas (Østerhus et al., 2019). The inflow of light surface waters from the North Atlantic to the Nordic Seas has instead increased (Årthun et al., 2019; Tsubouchi et al., 2021). More knowledge is needed to understand what mechanisms drive and influence the AMOC, as it is of great importance to make reliable climate predictions.

The sinking of dense water at high northern latitudes is not a driving mechanism of the AMOC, as it adds no energy to the system. Yet, it is important to sustain the overturning circulation, and it influences the volume transport and spatial extent of the AMOC (Kuhlbrodt et al., 2007; Bretones et al., 2022). It is also important for replenishing the deep ocean with oxygen, carbon, and other tracers (Fröb et al., 2016). Throughout this thesis, I will refer to the process where surface-water densifies and sinks as *overturning* or *dense-water formation*. The origins of the dense water sustaining the AMOC have been debated, and the prevailing view has gone through major revisions over the years. The main location of dense-water formation to supply the AMOC was long thought to be the Labrador Sea (Medhaug et al., 2012; Menary et al., 2015). To monitor the AMOC, the Overturning in the Subpolar North Atlantic Program (OSNAP) observing system was launched in 2014, deploying moorings along sections east and west of Greenland to observe the northward flow of light water, and the southward flow of dense water. Most of the overturning occurred east of Greenland, and thus the Labrador Sea was discarded as a major contributor of dense-water to the AMOC (Lozier et al., 2019). The Irminger Sea and the Iceland Basin were

instead suggested as important locations of dense-water formation to supply the AMOC (Petit et al., 2020), but Chafik and Rossby (2019) showed that the largest heat loss from the ocean to the atmosphere occurs farther north, in the Nordic Seas. The Nordic Seas have since been regarded as a major site of dense-water supply to the AMOC. In spite of constituting only 0.3% of the global-ocean volume, the Nordic Seas have substantial influence on the world's climate (Furevik et al., 2007).

1.2 The Nordic Seas

The Nordic Seas is the collective name for the Iceland, Greenland and Norwegian Seas. They are connected to the Arctic Ocean and the Barents Sea through the Fram Strait and the Barents Sea Opening, respectively. There are four sub-basins in the Nordic Seas; the Greenland Sea, the Iceland Sea, the Lofoten Basin, and the Norwegian Basin. The Greenland Sea is separated from the Lofoten Basin by the Mohn and Knipovich Ridges, and from the Iceland Sea by the West Jan Mayen Ridge. The Jan Mayen Ridge separates the Iceland Basin from the Norwegian Basin, and between the Norwegian Basin and Lofoten Basin lies the Vøring Spur. An overview of the bathymetry and general circulation of the Nordic Seas is shown in Figure 1.1. The Nordic Seas are separated from the North Atlantic by the Greenland-Scotland Ridge (GSR), yet dense water is allowed to pass from the Nordic Seas into the North Atlantic through gaps in the ridge. Water denser than $\sigma_\theta = 27.8 \, kg/m^3$ that spills from the Nordic Seas across the GSR is referred to as *overflow water*. As it crosses the ridge, it encounters the lighter water masses of the North Atlantic, and sinks into the abyss due to frictional forces. While sinking, it entrains ambient water and forms NADW. The Denmark Strait between Iceland and Greenland is an important gateway through which overflow water from the Nordic Seas enters the North Atlantic. With a sill depth of 630 m (Østerhus et al., 2019), about 3.2 Sv (1 $Sv = 10^6 \, m^3/s$) of overflow water flows through Denmark Strait, accounting for 60% of the total overflow across GSR (Harden et al., 2016; Jochumsen et al., 2017; Lin et al., 2020). The Faroe-Shetland Channel between the Faroe Islands and Scotland, with a sill depth of 840 m, is the other major overflow where 1.8 Sv of dense water enters the North Atlantic. The total overflow across GSR is estimated to 5.8 Sv (Østerhus et al., 2019).

At the surface, the Nordic Seas are dominated by warm and saline Atlantic Water (AW) in the eastern basins, and by cold and fresh Polar Water (PW) near the East Greenland shelf. These areas are referred to as the *Atlantic Domain* and the *Polar Domain* (Swift and Aagaard, 1981). Between the Atlantic and Polar Domains lies an area confined by pronounced hydrographic fronts towards east and west. Swift and Aagaard (1981) named this area the *Arctic Domain*. Most of the Greenland and Iceland Seas are part of the Arctic Domain. East of Iceland, the AW enters the Nordic Seas from the North Atlantic as the Norwegian Atlantic Current, an extension of the Gulf Stream. West of Iceland, AW enters the Nordic Seas with the North Icelandic Irminger Current (Figure 1.1). AW occupies the upper 400 - 600 m of the Norwegian and Lofoten Basins, overlying the colder and fresher Norwegian Sea Arctic Intermediate Water which enters the basins from the Greenland and Iceland Seas (Latarius and Quadfasel, 2016; Jeansson et al., 2017). As the Norwegian Atlantic Current continues northwards through the Norwegian Basin, it meets the Vøring Plateau and bifurcates into two branches: the Norwegian Atlantic Slope Current (NASC) and the Norwegian Atlantic Frontal Current (NAFC; Orvik and Niiler, 2002). The NASC follows the
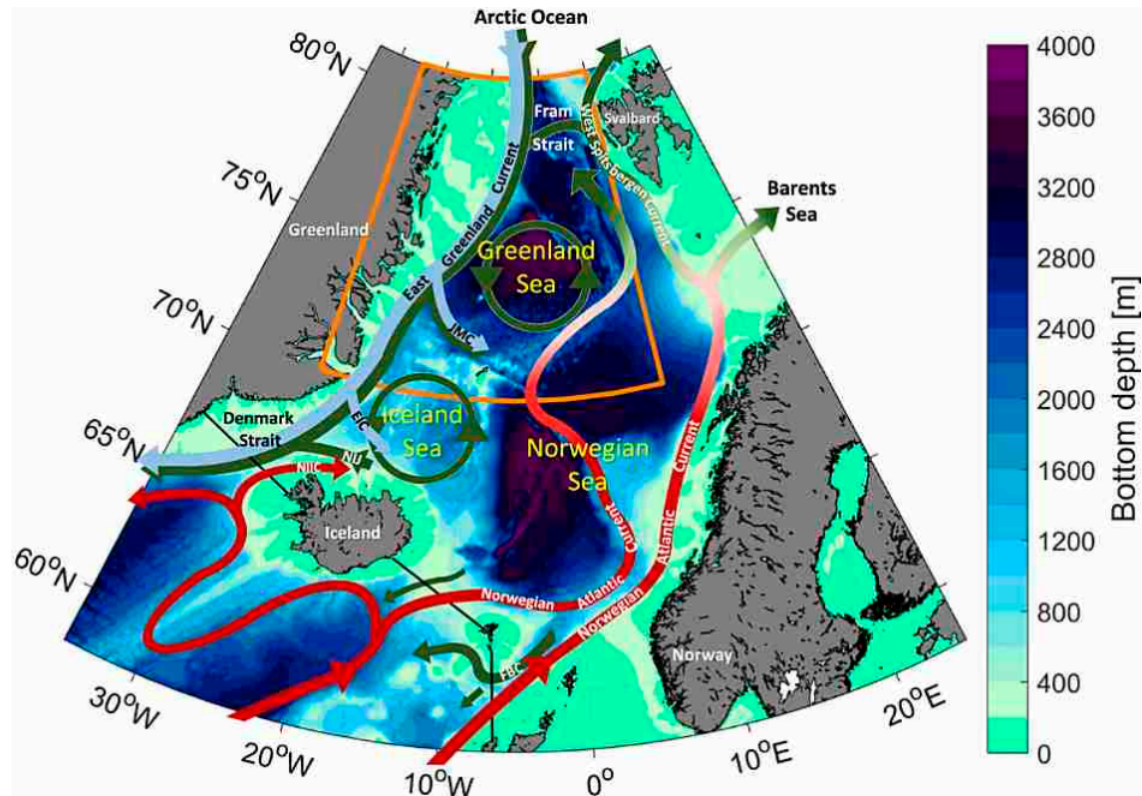
Figure 1.1: Circulation and bathymetry of the Nordic Seas, from Brakstad et al. (2019).

slope of the Norwegian Shelf. Some of it enters the Barents Sea through the Barents Sea Opening, before making its entrance to the Arctic Ocean. The rest continues towards Fram Strait as the West Spitsbergen Current (WSC). The NAFC is located at the hydrographic front between the Atlantic Domain and the Arctic Domain, following the Mohn and Knipovich Ridges. It reunites with the NASC (now the WSC) at Fram Strait. There, some of the AW enters the Arctic Ocean, to circulate until it re-enters the Nordic Seas as the intermediate water mass *Arctic Atlantic Water* (Mauritzen, 1996). The rest of the AW recirculates in Fram Strait, to continue along the slope of Greenland beneath the cold and fresh PW of the East Greenland Current (EGC). The EGC was long considered the only pathway for dense water to reach the Denmark Strait. In recent years, another pathway was discovered: the North Icelandic Jet originating along the Iceland slope (Jonsson and Valdimarsson, 2004; Våge et al., 2011; Semper et al., 2019). Two other recently discovered currents, the Iceland-Faroe Slope Jet (IFSJ; Semper et al., 2020) and the Faroe-Shetland Channel Jet (Chafik et al., 2020), transport dense water toward the Faroe-Shetland Channel along the Iceland-Scotland Ridge.

1.3   Overturning in the Nordic Seas

Historically, overturning in the Nordic Seas was thought to occur through open-ocean convection in the Arctic Domain (Swift et al., 1980; Swift and Aagaard, 1981; Strass et al., 1993). The Arctic Domain is an ideal place for open-ocean convection because of the low stratification and high atmospheric heat fluxes. Due to cyclonic circulation in the Greenland and Iceland Seas, isopycnals dome upward in the centres of the gyres, which brings dense water closer to the surface and reduces

stratification (Ronski and Budéus, 2005). In addition, proximity to the sea-ice edge enhances the formation of dense water, in particular during *cold-air outbreaks*. Cold-air outbreaks occur when cold and dry winds from sea-ice covered areas first encounter the relatively warm ocean. Close to the sea-ice edge, the ocean surface becomes subject to substantial heat loss to the atmosphere because of the strong temperature gradient. Up to 80% of the heat loss from the ocean to the atmosphere in the interior basins of the Nordic Seas occur during cold-air outbreaks (Papritz and Spengler, 2017), and water-mass transformation in these areas are thus greatly influenced by such events (Svingen et al., in prep; Våge et al., 2015). The gyres in the Greenland and Iceland Seas are in proximity of the ice edge, which makes them ideal locations for deep convection in terms of stratification and heat fluxes.

Mauritzen (1996) proposed a different scheme of overturning in the Nordic Seas. She argued that dense water was formed primarily through gradual cooling of AW within the boundary-current system, and that it was transported to the GSR by the EGC. She argued that dense-water formation in the interior basins could not be the main source of overflow water as there were no direct pathways from the interior basins toward the overflows. The convection in the interior basins also exhibits seasonal and interannual variability, which the overflow in Denmark Strait does not (Jochumsen et al., 2017). In addition, the largest heat loss to the atmosphere occurs in the Lofoten Basin (Isachsen et al., 2007), suggesting extensive water-mass transformation there. The discovery of the NIJ and the IFSJ revealed two additional pathways toward the North Atlantic. Both currents originate along the Iceland slope, and may transport water from the interior basins toward the overflows. The bulk of the water transported by the two currents have similar characteristics as that of dense water formed in the Greenland Sea. The Greenland Sea is therefore suggested as a potential source to the NIJ and IFSJ. Later studies have shown that water formed during winter in the Iceland Sea is mostly insufficiently dense to supply the NIJ and IFSJ (Våge et al., 2015). Today, the general consensus is that both the boundary-current system and the interior basins of the Nordic Seas supply the overflow water.

1.4   Overturning in the Greenland Sea

The densest water formed in the Nordic Seas originates in the Greenland Sea. Already in the early 1900s, Helland-Hansen and Nansen (1909) reported bottom-reaching convection in the Greenland Sea. Such bottom-reaching convection ventilating the entire water column was reported until the 1980s (Swift and Aagaard, 1981; Ronski and Budéus, 2005). The resulting product of this deep convection was Greenland Sea Deep Water (GSDW) and Greenland Sea Bottom Water (GSBW); fresh and very cold water masses that occupied most of the water column in the Greenland Sea, and contributed to the deep waters of the other basins of the Nordic Seas and Arctic Ocean.

The bottom-reaching convection ceased in the 1980s (Ronski and Budéus, 2005; Meincke et al., 1992), and only shallow ($< 300\,m$) convection took place until 1994 (Brakstad et al., 2019). The absence of deep-reaching convection allowed an intermediate temperature maximum to develop, increasing the stratification at intermediate depths (Figure 1.2). The maximum was pushed deeper in the water column as convection occured, but no convective event has been strong enough to completely erode it. The maximum prevents the formation of GSDW and GSBW, which have not been produced since the emergence of the maximum. Another water mass is now the main

product of the Greenland Sea: the Greenland Sea Arctic Intermediate Water (GSAIW; Brakstad et al., 2019). Located between 500 m and the stratification maximum in the water column, it is lighter than the GSDW, but still the densest local product of the Nordic Seas. The GSAIW may be more important to the overflow across GSR than the GSDW was, as the latter may have been too dense to cross the shallow sills in the ridge. The GSAIW is thought to supply the densest portion of overflow water across GSR (Huang et al., 2020).
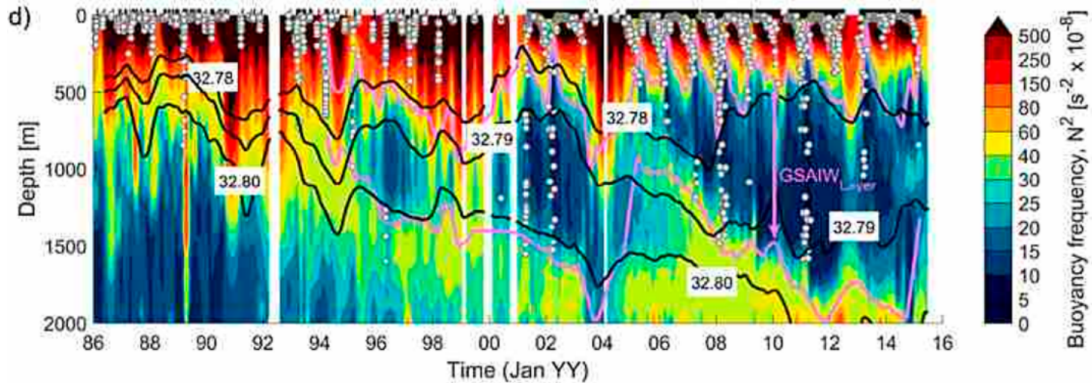

Figure 1.2: Evolution of the buoyancy frequency from 1986 to 2016, with contours of potential density anomaly referrenced to 1000 m in black (from Brakstad et al., 2019)

1.5   Motivation

As the atmospheric temperature rises faster than the ocean temperature, the temperature gradient between the ocean and atmosphere is reduced. Sea ice retreats, and so does the location of the cold-air outbreaks. The wintertime air-sea heat fluxes in the Greenland and Iceland Seas were reduced by 20% between 1979 and 2015 (Moore et al., 2015). This motivates the question: how will climate change affect the overturning in the Nordic Seas, and what will be the consequences for the AMOC? Some models predict that dense-water formation will diminish as the sea-ice edge retreats, and future dense-water supply to the AMOC may shift northward into the Arctic Ocean (Bretones et al., 2022). To better predict future dense-water formation, knowledge and understanding about the present state is needed. Observations are sparse in the Nordic Seas compared to lower latitudes due to rough wintertime conditions. Models and reanalyses provide information where observations are lacking, and increase our knowledge about the sparsly-sampled oceans. Models have the disadvantage that they are unsupported by observations, and reanalyses have the disadvantage that they contain artificial sources and sinks to force an optimal fit with observations. A state estimate, on the other hand, is guided by observations while being obedient to physical laws. The *Arctic Subpolar gyre sTate Estimate* (ASTE; Nguyen et al., 2021) is the first Arctic-focused state estimate, and it includes the majority of observations made between 2002 and 2017 in the Arctic Ocean and adjacent seas. As its predecessor *Estimating the Circulation and Climate of the Ocean* (ECCO; Forget et al., 2015), it satisfies the laws of physics and thus conserves heat, salt, volume, and momentum. This makes the state estimate an ideal tool for investigating the overturning in the Nordic Seas.

In this thesis, I will utilize ASTE to address the overturning in the Nordic Seas. As the state

estimate has not yet been evaluated or utilized in the Nordic Seas, this is novel work. The thesis is divided into two main parts; the first is an evaluation of ASTE in the Nordic Seas, and the second is an investigation of the overturning in the Nordic Seas from 2002 to 2017 in the state estimate. In particular, I will attempt to address the following questions: How well does ASTE reproduce the main features of the Nordic Seas? How much dense water is formed in the Nordic Seas? Where is the dense water formed, and what influences the formation of dense water?

2 | **Theory**

Dense-water formation and sinking of dense water in the North Atlantic are required to maintain the AMOC. This chapter is dedicated to describing the two processes, which are connected, but not synonymous.

2.1   Dense-water formation

The density of seawater is dependent on temperature, salinity, and pressure, expressed by the equation of state:

$$\rho = \rho\left(T, S, p\right) \tag{2.1}$$

Here, ρ is density, T is temperature, S is salinity, and p is pressure. The equation is often simplified to the form

$$\rho = \rho_0[1 - \alpha_T(T - T_0) + \beta_S(S - S_0)] \tag{2.2}$$

where α_T and β_S are the thermal expansion coefficient and the haline contraction coefficient, respectively, and T_0 and S_0 are reference values of temperature and salinity. The coefficients α_T and β_S are often treated as constants, yet they vary with temperature and pressure (Marshall and Schott, 1999) and care is needed when applying the equation.

There are two ways of increasing the density of sea water at the surface: by increasing its salinity and by decreasing its temperature (Equation 2.2). Both mechanisms are important in dense-water formation. In Antarctica, increased density due to increased salinity from sea-ice formation is an important factor in forming the bottom water occupying the abyss of the world oceans, called Antarctic Bottom Water (Nicholls et al., 2009). On the shallow shelves around the Arctic Ocean, sea-ice formation drastically increases the salinity of the underlying, shallow water column, which in turn spills down into the deep basins as dense plumes of high salinity (Jones et al., 1995; Swift and Aagaard, 1981). In the Nordic Seas, however, atmospheric cooling in winter is the main mechanism that produces dense water.

In the interior basins of the Nordic Seas, atmospheric cooling can induce open-ocean convection. Open-ocean convection is a process where the ocean surface is cooled by the atmosphere to an extent where it exceeds the density of the underlying water. The water column becomes unstable, and convective plumes start to form. The plumes are of small horizontal scale ($< 1\ km$), and move downward with vertical velocities up to 10 cm/s (Marshall and Schott, 1999). The plumes efficiently mix the water column down to the depth at which they encounter water with higher densities. This depth is referred to as the *mixed-layer depth* or the *convection depth*. The water above the convection depth, the *mixed layer*, is well mixed and characterized by low stratification.

When considering areas larger than the scale of the convective plumes, open-ocean convection does not necessarily lead to net sinking of water - it is rather a process of densification and vertical mixing. When cooling diminishes, convection stops and the water column restratifies (Marshall and Schott, 1999).

The depth of convection is not only dependent on the amount of atmospheric cooling of the ocean surface, but also by the stratification of the water column, given by

$$N^2 = \frac{g}{\rho_0} \frac{\delta \rho}{\delta z} \tag{2.3}$$

where N^2 is a measure of the frequency of internal waves, called the buoyancy frequency, g is the acceleration due to gravity, and $\frac{\delta \rho}{\delta z}$ is the vertical stratification of the water column. Ideal locations for open-ocean convection tend to be preconditioned with a weakly-stratified water column beneath the pycnocline before the onset of wintertime cooling. Cyclonic circulation is also favourable for deep open-ocean convection. Cyclonic circulation causes isopycnal doming due to Ekman-divergence in the Ekman layer, lifting dense water closer to the surface. The stratification then decreases and the weakly stratified interior of the basin is brought closer to the surface and becomes more readily exposed to the atmosphere. The surface salinity prior to the winter cooling is also of importance (e.g. Brakstad et al., 2019). If the surface water is too fresh, cooling will result in formation of sea ice rather than densification of the water. Sea ice efficiently isolates the underlying water from the atmospheric forcing, and thus inhibits dense-water formation. In today's climate, open-ocean convection is confined to the Nordic Seas, the Labrador Sea, the Irminger Sea, and the Mediterranean Sea. Open-ocean convection has also been observed occasionally in the Weddell Sea. In this thesis, I will exclusively address overturning in the Nordic Seas.

Open-ocean convection is not the only process through which dense water is produced in the Nordic Seas, dense water is also formed in the boundary-current system. A schematic of the two processes is shown in Figure 2.1. The warm AW that enters the Nordic Seas quickly loses heat to the atmosphere as it proceeds northward, especially in the Lofoten Basin where the atmospheric forcing is largest (Isachsen et al., 2007). Water in the boundary-current system may also cool as a result of eddy exchange between the current and the colder interior basins, depending on the baroclinicity of the current. The NAFC is baroclinic, moving northward with the cold and dense waters of the Greenland Sea to the west. Isopycnals tilt upwards towards the Greenland Sea. Eddies smooth the density differences and thus flatten the isopycnic slope. The current in turn becomes less baroclinic, and the vertical velocity shear is reduced - meaning that surface velocities are reduced while velocities at depth increase. This, in turn, leads to a horizontal convergence in the surface layers and a horizontal divergence at depth, which is compensated by downwelling. In such terms, densification of water along the boundary-current system of the Nordic Seas also results in a net sinking of water (Johnson et al., 2019).
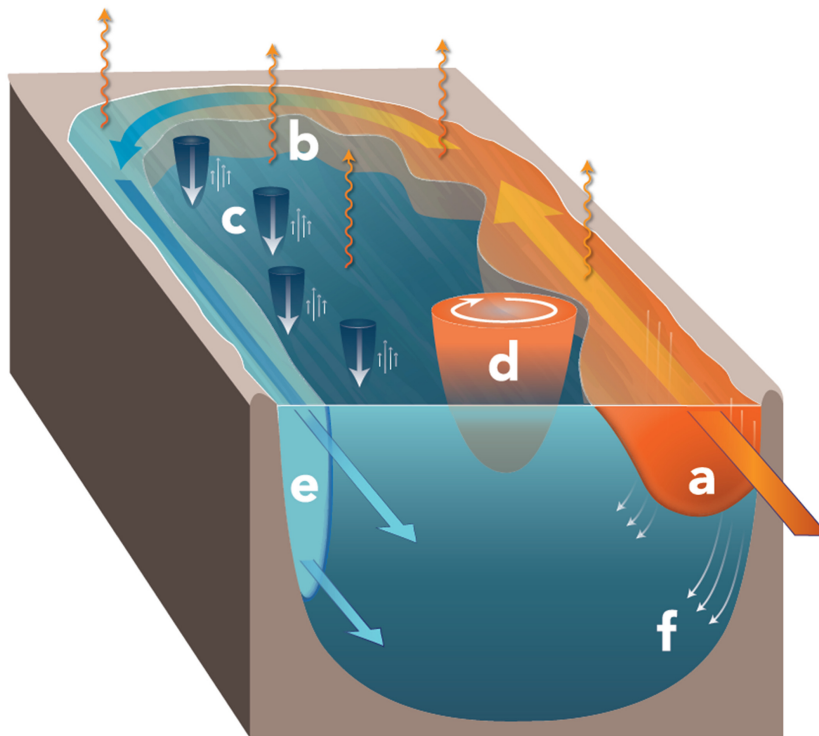
Figure 2.1: Schematic illustrating dense-water formation and sinking in the boundary-current system and in the interior basins: a) inflow of warm water at surface, b) atmospheric cooling, c) convective plumes, d) eddy activity, e) outflow of cooled, dense water and f) downwelling along the boundaries (from Johnson et al. ,2019)

3 | Data and Methods

In this chapter I will describe the Arctic Subpolar gyre sTate Estimate, which is the main subject of my analysis. I will also introduce the different observational datasets used to evaluate the state estimate, as well as the method used to quantify water-mass transformation.
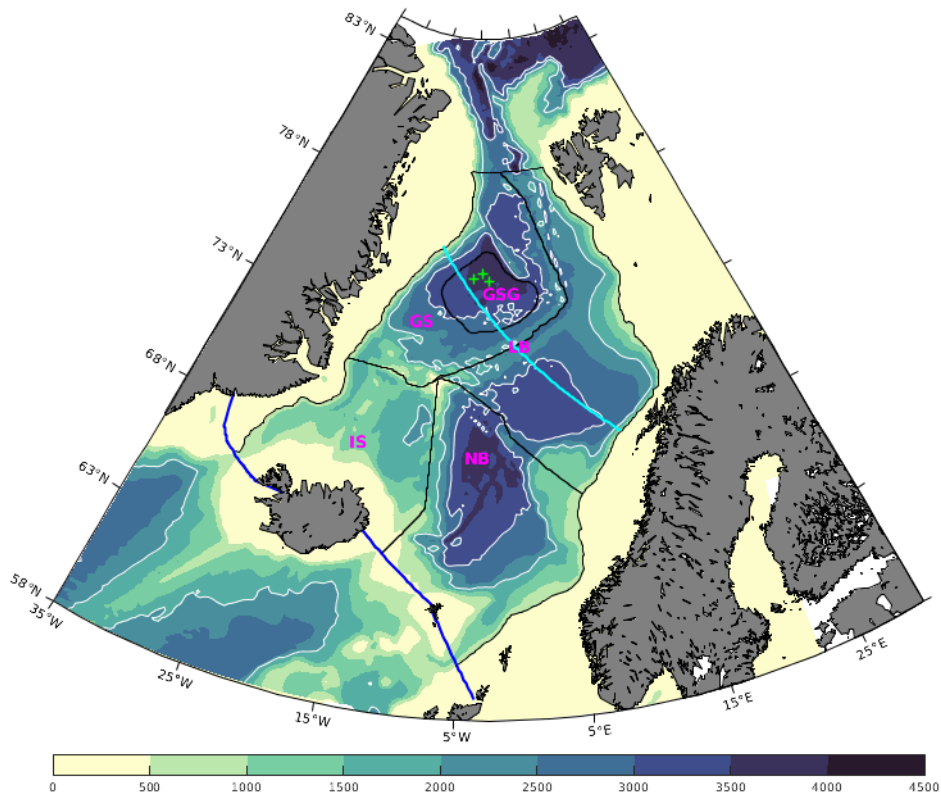

Figure 3.1: Bathymetry and basins of the Nordic Seas. The black contours show the outlines of the Greenland Sea (GS), the Greenland Sea Gyre (GSG), the Iceland Sea (IS), the Lofoten Basin (LB) and the Norwegian Basin (NB). The green crosses show the location of the three moorings. The cyan and blue lines show the positions of the Greenland Sea - Lofoten Basin section and the GSR section, respectively.

3.1 The Arctic Subpolar gyre sTate Estimate

ASTE is a medium-resolution ocean state estimate of the Arctic Ocean and surrounding seas between 2002 and 2017 (Nguyen et al., 2021). It is based on the global ECCO (Forget et al., 2015) which, because of its coarser resolution and the sparse sampling of the Arctic region compared to lower latitudes, resulted in large biases there. ASTE is not the first data-constrained product

in the Arctic region, as several ocean reanalyses exist (e.g. C-GLORS025v5, ECDA3, GECCO2, Glorys2v4, GloSea5-GO5, MOVE-G2i, ORAP5, SODA3.3.1, TOPAZ4 and UR025.4; Uotila et al., 2019). Yet, as the first Arctic-focused ocean state estimate, ASTE has a valuable advantage compared to the reanalyses: it is strictly obedient to physical laws and is thus free of artificial sources and sinks.
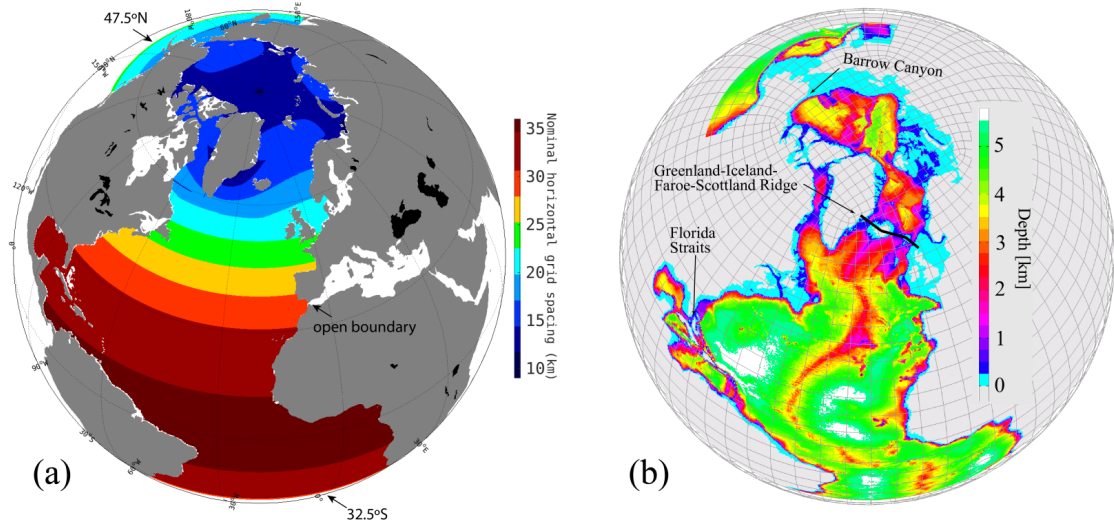

Figure 3.2: (a) Horizontal grid spacing and (b) bathymetry in ASTE (from Nguyen et al., 2021)

As ECCO, ASTE is based on the Massachusetts Institute of Technology General Circulation Model (MITgcm), which solves the primitive equations in re-scaled z-coordinates using a nonlinear free surface. With horizontal grid spacing of $1/3°$(corresponding to approximately 16 km in the Nordic Seas), ASTE's resolution is higher than that of ECCOv4r3 ($1°$). Still, it is not sufficiently high to resolve the Rossby radius of deformation in the Nordic Seas, which is generally small due to the weak stratification and the high latitudes (Nurser and Bacon, 2014). The state estimate has 50 unevenly-spaced vertical levels with thicknesses ranging from 10 m near the surface to 500 m in the abyss. ASTE's domain covers the Atlantic Ocean north of $32.5°S$, the Labrador Sea, the Nordic Seas, the Barents Sea, the Canadian Archipelago, the Arctic Ocean, and the Bering Sea north of $47.5°N$ (Figure 3.2a).

The bathymetry used in ASTE is a combination of the bathymetry data created and provided by (Smith and Sandwell, 1997; version 14.1) south of $60°N$ and the international bathymetric chart of the Arctic Ocean (IBCAO; Jakobsson et al., 2012) north of $60°N$. The two are blended over a range of 200 km centered around this latitude, with special care taken to remove abrupt transitions. Model depths in particularly critical regions, such as the Greenland-Scotland Ridge, are forced to agree with observations (Figure 3.2b).

Output from ECCOv4r3 is used as lateral boundary conditions, but not to initialize the model due to the large errors in the Arctic Ocean. Instead, existing estimates based on observations and models are selected as first-guess model input parameters (albedo of sea ice and snow, drag coefficients, mixing and dissipation parameters, velocity, thickness and concentration of sea ice,
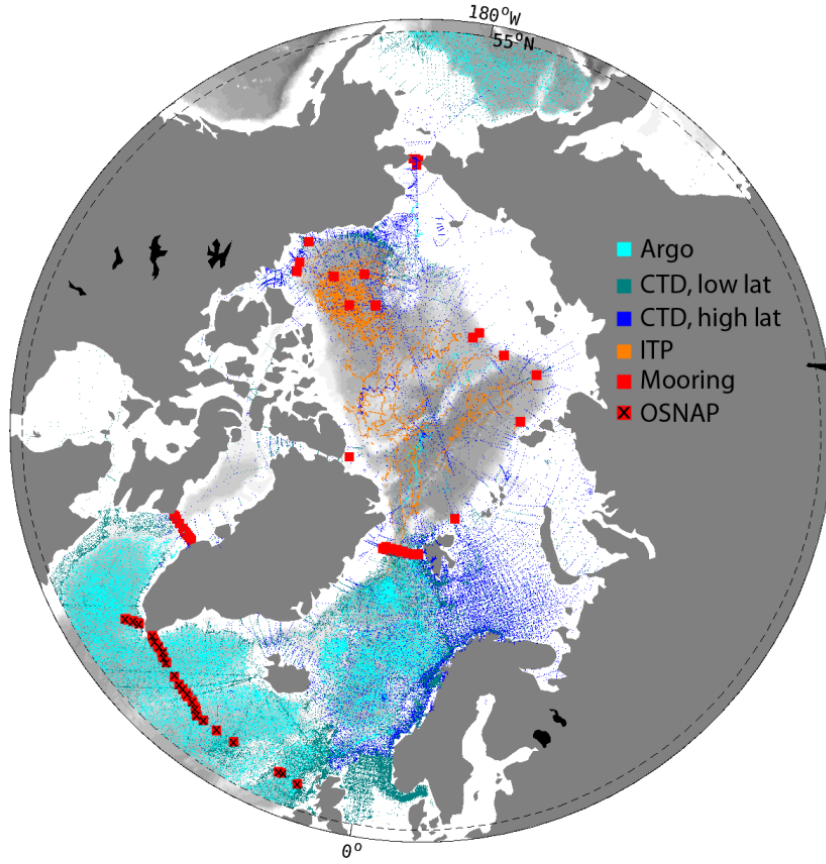
Figure 3.3: In situ data used in ASTE (from Nguyen et al., 2021).

and salinity, temperature, and velocity of the ocean). The model was spun up for 6 years with repeated atmospheric forcing and open boundary conditions from 2002, and the ocean state at the end of these 6 years was used as initial conditions for ASTE. The atmospheric forcing applied to ASTE is provided by the atmospheric reanalysis JRA-55 made by The Japan Meteorological Agency, as it has previously shown to result in reasonable sea-ice concentrations in the Arctic Ocean (Nguyen et al., 2011). The forcing is applied through the bulk formulae over the open ocean. Freshwater fluxes from river runoff are taken from the Regional, Electronic, Hydrographic Data Network for the Arctic Region (R-ArcticNET) dataset.

The solution was then constrained by over 10^9 satellite and in situ observations (see Figure 3.3), through gradient-based iterative least-squared minimization of the *cost function*, which describes the misfit between the model and data:

$$J = \sum_{t=t_0+\Delta t}^{t_f} [y(t) - E(t)x(t)]^T R(t)^{-1}[y(t) - E(t)x(t)]$$
$$+ [x_0 - x(t_0)]^T B(t_0)^{-1}[x_0 - x(t_0)]$$
$$+ \sum_{t=t_0}^{t_f - \Delta t} u(t)^T Q(t)^{-1} u(t)$$

where t_0 and t_f are the initial and final time, Δt is the time-step, $y(t)$ is the observation vector, $x(t)$ is the state vector containing the model solution at all grid points, x_0 is the initial guess and

$x(t_0)$ is the initial state. E is the operator mapping the state variables to the observations, and the model-data misfit $y(t) - E(t)x(t)$ is weighted by the inverse error covariance $R(t)$. $B(t_0)$ and $Q(t)$ are error covariances of x_0 and $u(t)$ respectively, and u is the parameter adjustment.

The cost function includes three major contributions. The first term is the normalized squared model-data misfit that is to be minimized. The second term gives less weight to the initial guess if the deviation of the initial state from the initial guess is large, and the third term moderates the amplitude of the input parameter adjustments. This is to make sure that the input parameters are not adjusted to exceed their expected ranges (Nguyen et al., 2021).

The mixed-layer depths in ASTE are calculated following a procedure by Kara et al. (2000), which determines the vertical extent of the mixed-layer by the depth where the density increases by $\Delta\rho$ compared to the density at 10 m depth:

$$\Delta\rho = \rho(T + \Delta T, S, P) - \rho(T, S, P)$$

where ρ is density, T is temperaure, S is salinity, and P is pressure. In ASTE, $\Delta T = 0.8°C$ is used as criterion.

3.2 Observations

Various observational datasets were used to evaluate the performance of ASTE in the Nordic Seas. They will be introduced in the following.

Hydrographic climatology

The late-winter (February - April) hydrographic climatology from 2000 to 2019 (Brakstad et al., in prep) consists of data collected from several sources, including the Unified Database for Arctic and Subarctic Hydrography (UDASH), the International Council for the Exploration of the Seas (ICES), the Marine Freshwater and Research Institute of Iceland, the World Ocean Database (WOD), the Global Ocean Data Analysis Project version 2 (Glodapv2), the Argo Program, the Norwegian Iceland Seas Experiment (NISE), the Institute of Marine Research (IMR), the Iceland-Greenland Seas Project, and shipboard measurements along the continental slope of Iceland. The data was combined and quality controlled, the control including removing duplicates, density inversions exceeding 0.05 kg/m^3, and data outside the expected range of 0 - 36 g/kg and -2 - 30 °C for salinity and temperature, respectively. Data from 2000 to 2019 were interpolated onto a three-dimensional grid with zonal resolution of 1/3°, meridional resolution of 1/8°, and 46 unevenly spaced vertical grid points (Brakstad et al., in prep).

The dataset represents late-winter hydrography, yet late-winter observations have not been obtained at all locations, and some adjustments were needed to represent realistic winter mixed layers (Brakstad et al., in prep). The mixed-layer depths from Brakstad et al. (2019) and Våge et al. (2015) were used in the Greenland and Iceland Seas, respectively. At locations where only summer profiles were obtained, late-winter mixed layers from nearby profiles were applied while keeping the summer profile beneath the the mixed-layer depth. Mixed-layer depths in the remaining parts of the domain were estimated from the late-winter profiles using a procedure from Nilsen and Falck (2006), which identifies the base of the mixed layer in a manner similar to

that used in ASTE (Kara et al., 2000). Following Våge et al. (2015) and Brakstad et al. (2019), the density difference criterion was set to $\Delta T = 0.2°C$ instead of $\Delta T = 0.8°C$ due to the low stratification in the area.

Moored time series from the central Greenland Sea

In an attempt to evaluate ASTE's temporal evolution, the results are compared to independent moored measurements in the central Greenland Sea. The measurements stems from three moorings that were deployed annually in the central Greenland Sea between 1999 and 2009 (Svingen et al., in prep). This dataset overlaps with the time period of ASTE from 2002 to 2009, and thus provides 8 years of direct comparison. The dataset is published in Pangaea (`https://doi.org/10.1594/PANGAEA.911001`).
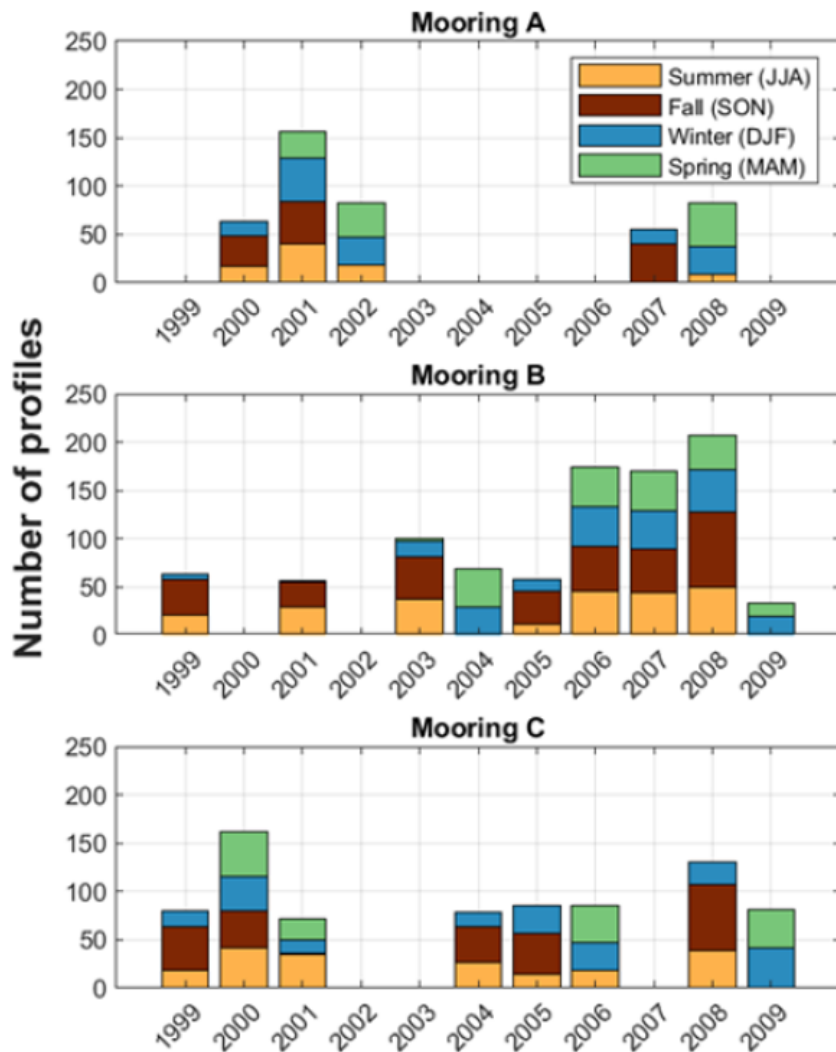

Figure 3.4: Annual number of profiles per deployment at each mooring site, color coded by season (from Svingen et al., in prep)

The three moorings were deployed inside the Greenland Sea Gyre, between 2°30' W and 4°37' W, and 74°50' N and 75°05' N (Figure 3.1). Each of the moorings was equipped with a profiling vehicle, measuring conductivity, temperature, and pressure every second day, with some

gaps in 2002, 2003, and 2005 (Figure 3.4). The data were calibrated annually to shipboard CTD measurements, interpolated to integer pressure values, and smoothed with a 10-m running mean (Svingen et al., in prep). Temperature and salinity data outside the range of -2°C - 20°C and 20-36 were excluded respectively. Data from unsuccessful casts, where the moored profiler was parked at constant depth, were removed. The data were converted from practical salinity and potential temperature to absolute salinity and conservative temperature according to the International Thermodynamic Equation of Seawater - 2010 (TEOS-2010; IOC et al.,2010). As the output from ASTE is presented following the Climate and Forecast Metadata Convention version 1.6, I used the Gibbs-SeaWater (GSW) Oceanographic Toolbox to re-convert the data for direct comparison.

Mixed-layer depths were estimated using two routines: the routine from Nilsen and Falck (2006) and a routine from Lorbacher et al. (2006). The routine from Lorbacher et al. (2006) estimates the base of the mixed-layer where the temperature profile has a curvature extremum. All the profiles were then visually insepcted, and were neither of the two procedures correctly identified the base of the mixed layer, a manual procedure was applied (Pickart et al., 2002). In this procedure, the top and bottom depths of the mixed-layer are estimated visually and the means and standard deviations of salinity, temperature and density are calculated between the two depths. The extent of the mixed layer are then defined where the density profile exceeds two standard deviations from the calculated means.

Surface geostrophic velocity

The surface geostrophic velocities are provided by Copernicus (`https://doi.org/10.48670/moi-00148`), derived from altimeter satellite sea level anomalies with respect to a twenty year mean. The product contains data from several altimeter missions (Jason-3, Sentinel-3A, HY-2A, Saral/AltiKa,Cryosat-2, Jason-2, Jason-1, T/P, ENVISAT, GFO,ERS1/2) which were regridded onto a $0.25° \times 0.25°$ grid and processed by the DUACS multimission altimeter data processingsystem.

3.3 Quantifying water-mass transformation

To address water mass transformation in the Nordic Seas, I defined five domains within the Nordic Seas which were used as control volumes: the Greenland Sea, the central Greenland Sea (the Greenland Sea Gyre), the Iceland Sea, the Lofoten Basin, and the Norwegian Basin (Figure 3.1).

Using density anomaly levels of $\sigma_\theta(j)$ where $j = 1, 2, ..., J$ separated by $\Delta\sigma_\theta = 0.04 kg/m^3$ and within the range of $27.00 - 29.00 \ kg/m^3$ in such a way that

$$\sigma_\theta(j = 1, j = 2, j = 3, ... j = J) = 27.00, 27.04, 27.08, ..., 29.00$$

I defined density classes $D(j_1, j_2, j_3, ..., j_{J-1})$ so that the upper and lower density limit of $D(j)$ was $\sigma_\theta < \sigma_\theta(j + 1)$ and $\sigma_\theta \leq \sigma_\theta(j)$, respectively.

The output from ASTE has zonal dimension $x(i_1)$ where $i_1 \in [1, X]$, meridional dimension $y(i_2)$ where $i_2 \in [1, Y]$, vertical dimension $z(i_3)$ where $i_3 \in [1, Z]$ and temporal dimension $t(i_4)$ where

$i_4 \in [1, T]$. The estimated density $\sigma_{ASTE}(x, y, z, t)$ of each grid cell within the control volume of interest at each time step was then addressed the appropriate density class D by checking if it satisfied the following condition:

$$\sigma_\theta(j - 0.005) \le \sigma_{ASTE}(i_1, i_2, i_3, i_4) < \sigma_\theta(j + 1.005)$$

If it did, the corresponding grid cell volume $v_{ASTE}(i_1, i_2, i_3, i_4)$ was added to a matrix $V(t, \sigma_\theta)$ so that

$$V(i_4, j) = v(i_1, i_2, i_3, i_4) + V(i_4, j)$$

This results in a volume matrix $V(t, \sigma_\theta)$ with one dimension σ_θ with length J equal to the number of density classes and one dimension with length T equal to the number of time steps. It contains the total volume constituted by each density class at each time step inside the control volume. In an attempt to reduce the sensitivity of V to the chosen values of σ_θ, I utilized an overlap of $0.01 kg/m^3$ when addressing values to the belonging density class. The resulting excess volume was controlled for.

To examine the horizontal distribution of volume in each density class, the procedure was repeated using a volume matrix $V(x, y, t)$ so that

$$V(i_1, i_2, i_4) = v(i_1, i_2, i_3, i_4) + V(i_1, i_2, i_4).$$

4 | Evaluating ASTE in the Nordic Seas

All figures in this chapter, unless stated otherwise, show data from February, March, and April. I will refer to these months as *late winter*. The figures show fall or late-winter values averaged over several years. The output from ASTE is averaged over the entire ASTE period, from 2002 to 2017. The observations are averaged from 2000 to 2019. In the following sections, the mean late-winter potential temperature, salinity, potential density anomaly, and mixed-layer depths will be referred to simply as temperature, salinity, mixed-layer depth, and density.

4.1   Mean late-winter hydrography

Surface salinity and surface temperature in the Nordic Seas are shown in Figures 4.1 and 4.2. ASTE reproduces the main surface hydrographic features of the Nordic Seas to the extent that warm, saline AW enters the domain from the North Atlantic east and west of Iceland, and cold and fresh PW enters through Fram Strait with the EGC. The warm and saline AW spreads horizontally across the Lofoten and Norwegian Basins. This indicates the division of the North Atlantic Current into the NAFC and the NASC. The warm, saline water also extends into the Barents Sea through the Barents Sea Opening, and the Arctic Ocean through Fram Strait - indicating the bifurcation of the NASC into the WSC and an eastern Barents Sea branch.
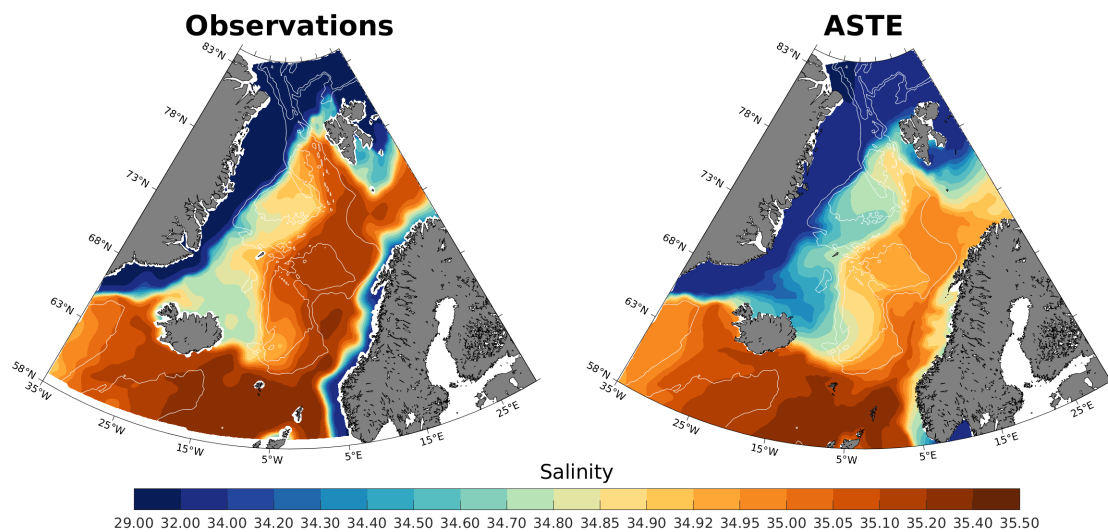

Figure 4.1: Surface salinity from observations (left panel) and ASTE (right panel).
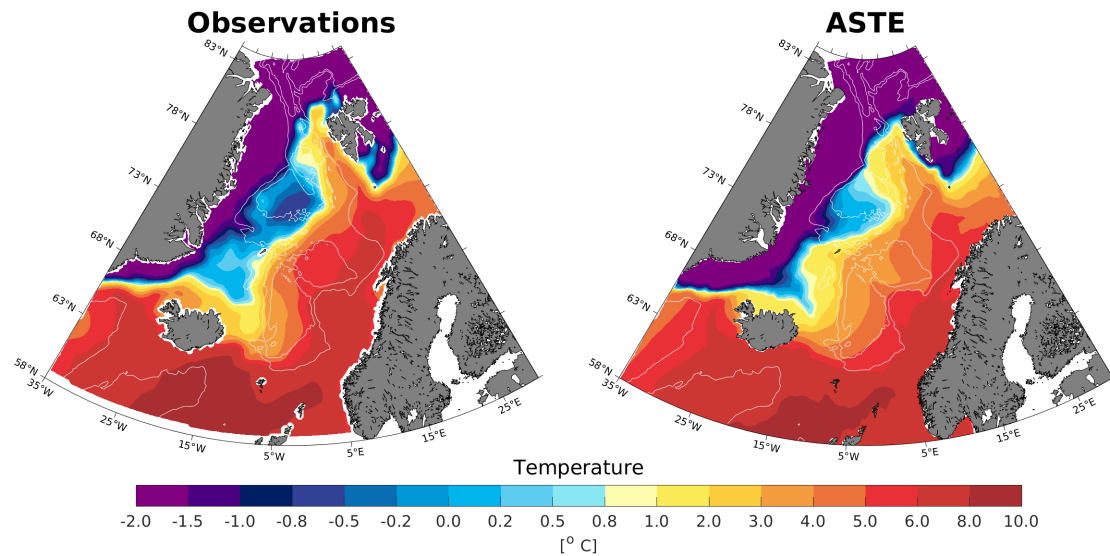
Figure 4.2: Surface temperature from observations (left panel) and ASTE (right panel).
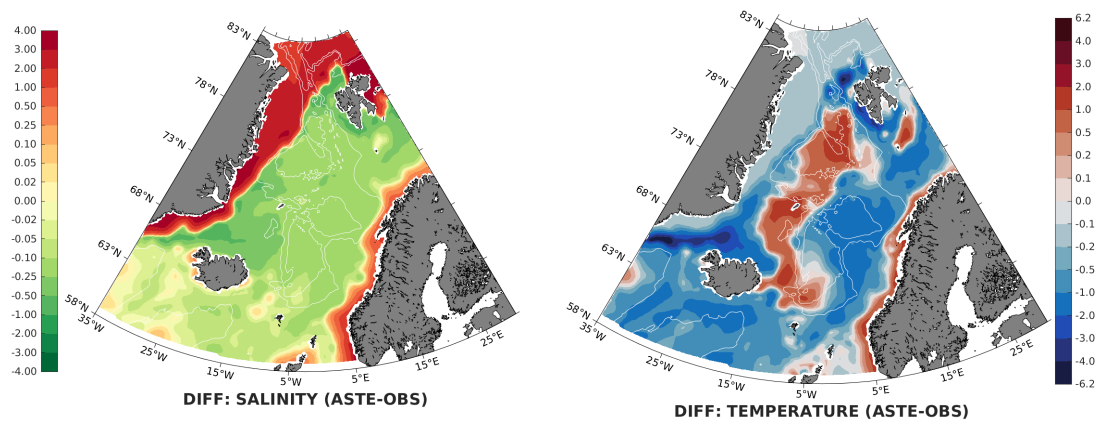

Figure 4.3: Difference between observations and ASTE in salinity (left panel) and temperature (right panel) at the surface. Note the nonlinear color scale.

However, the discrepansies between model and observations appear clearly in Figure 4.3. In ASTE, the salinities of the EGC and the Norwegian Coastal Current are overestimated by values up to 4. This is a remarkable difference, but observations on the East Greenland shelf are sparse in winter, and thus the difference is uncertain. Apart from the EGC and the Norwegian Coastal Current, the rest of the surface waters in the Nordic Seas are slightly fresher in ASTE than in the observations, by approximately 0.25 (Figure 4.3). The output from ASTE is generally colder than the observations, by around 1°C. The exceptions are the Arctic Domain and the Norwegian Coastal Current, which are up to 4°C warmer. The differences in surface temperature are mainly due to ASTE's too smooth and wide representation of the hydrographic front between the Atlantic and Arctic Domains. In ASTE, the warm AW is allowed to cross the Jan Mayen and Mohn Ridges, while the bathymetry appears to present a more pronounced barrier in the observations. The differences in salinity between ASTE and observations in the EGC and Norwegian Coastal Current may be caused by ASTE's resolution. The horizontal resolution of 16 km is too coarse to resolve the freshwater runoff into the fjords of Greenland and Norway, which are of smaller scale. This leads to biases also in the Arctic Ocean (Nguyen et al., 2021).
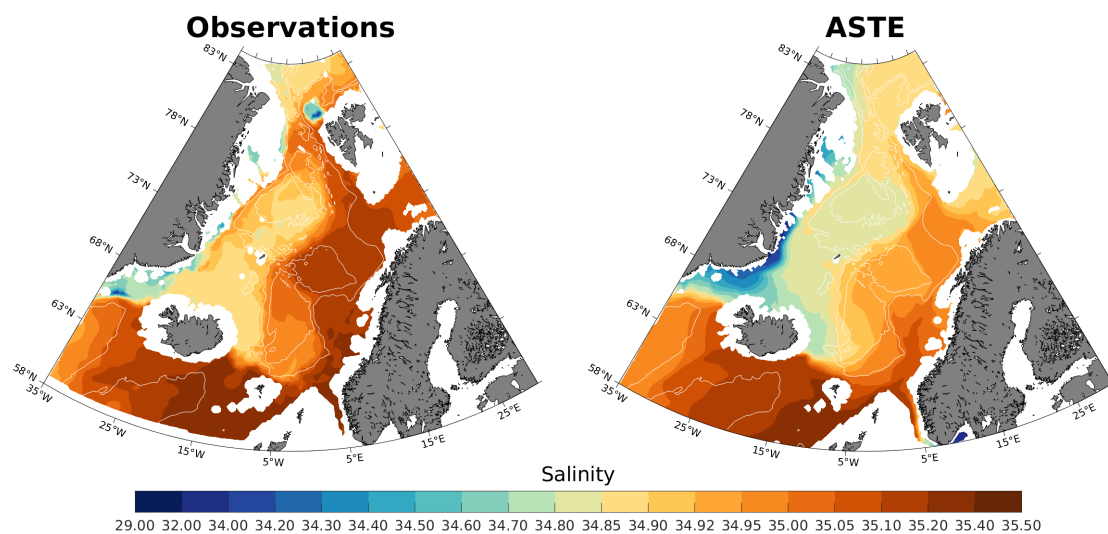
Observations   **ASTE**

Salinity

29.00 32.00 34.00 34.20 34.30 34.40 34.50 34.60 34.70 34.80 34.85 34.90 34.92 34.95 35.00 35.05 35.10 35.20 35.40 35.50

Figure 4.4: Salinity at 250 m depth from observations (left panel) and ASTE (right panel).

Observations   **ASTE**

Temperature

-2.0 -1.5 -1.0 -0.8 -0.5 -0.2 0.0 0.2 0.5 0.8 1.0 2.0 3.0 4.0 5.0 6.0 8.0 10.0
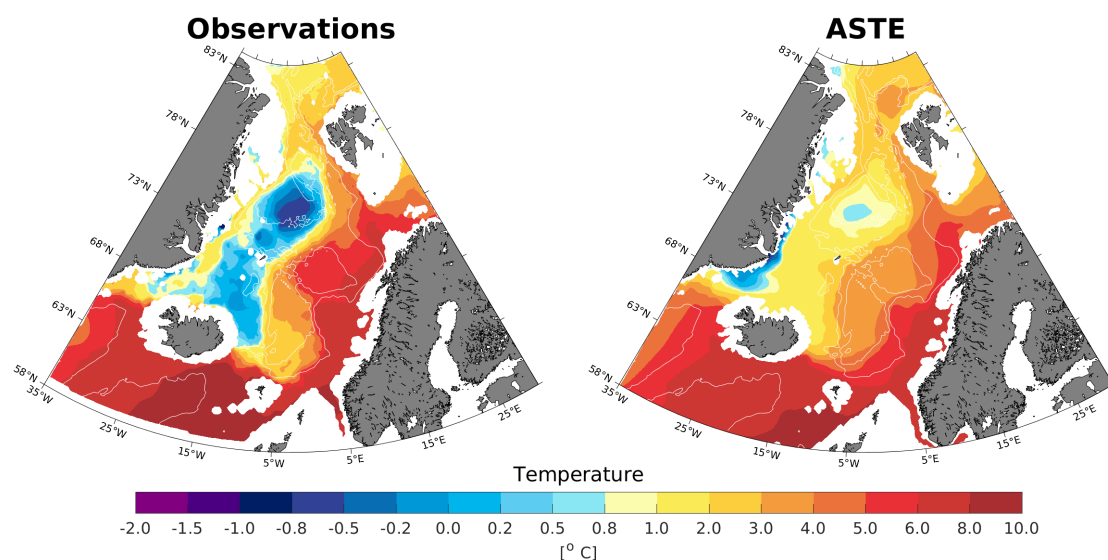
[°C]

Figure 4.5: Temperature at 250 m depth, from observations (left panel) and ASTE (right panel).

At 250 m depth, the absolute differences in salinity are reduced, and most of the domain is too fresh by values between 0.02 and 0.10 (Figures 4.4 and 4.6). While the surface temperature was overestimated mostly in the Arctic Domain, the temperature in the western part of the Norwegian Basin is also estimated high at 250 m (Figure 4.5). The temperatures in the Greenland Sea, Iceland Sea, and Norwegian Basin are overestimated by approximately 2°C, while the surrounding areas are too cold by approximately 1°C .The pattern seems to be connected to the different water masses: the inflowing AW is generally too cold, while the ambient water is too warm.

At 500 m depth, the ASTE salinity is further improved in three of the basins of the Nordic Seas, the exception being the Lofoten Basin which is still too fresh by 0.25. In the rest of the domain, differences between ASTE and observations are less than 0.05 (see Figures 4.7 and 4.9).
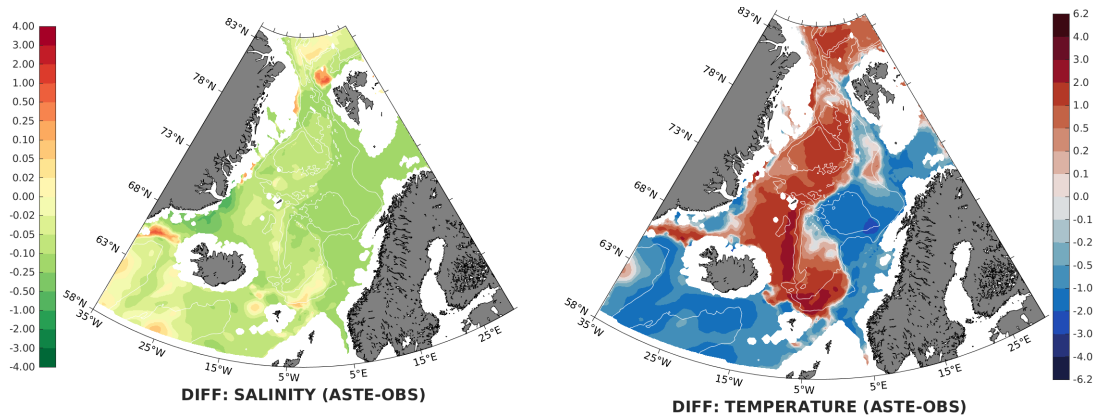
Figure 4.6: Difference between observations and ASTE in salinity (left panel) and temperature (right panel) at 250 m depth. Note the nonlinear color scale.
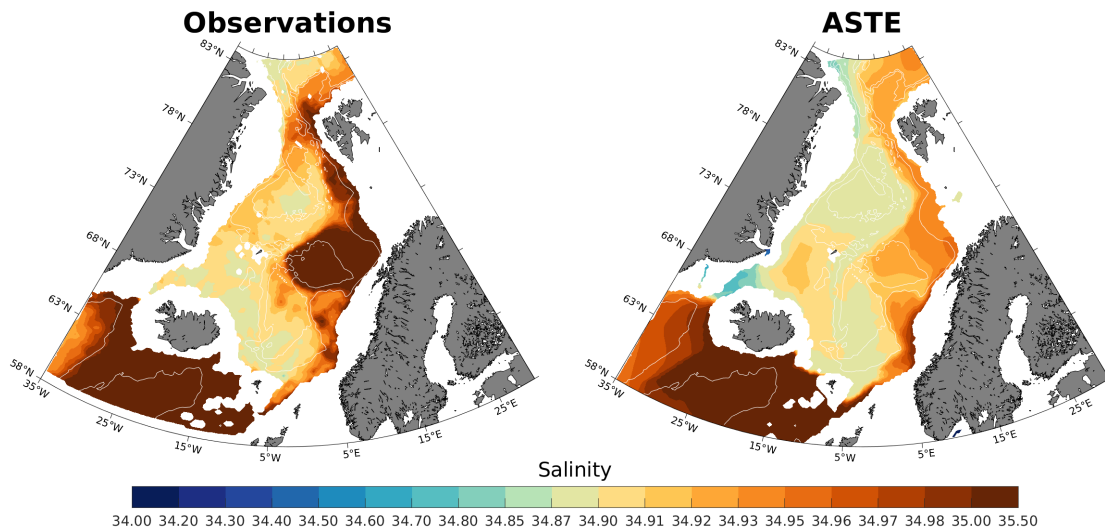

Figure 4.7: Salinity at 500 m depth from observations (left panel) and ASTE (right panel).

The temperature is overestimated by up to 2°C almost everywhere north of the GSR (Figures 4.8 and 4.9), the exception being the Lofoten Basin where the temperature is too cold by up to 4°C. The warm, fresh bias in ASTE increases down to 500 m depth. The signal seems to follow the spreading of locally formed intermediate water, a product of convection in the Arctic Domain. The process of convection is often poorly resolved in models, and its product tends to be biased towards lower densities (Heuzé, 2021).

At 1000 m, ASTE generally estimates the temperature and salinity better compared to shallower depths (Figures 4.10, 4.11 and 4.12). Salinity is slightly overestimated in almost the entire domain by values up to 0.025, while temperature is generally overestimated by 0.2°C everywhere except in the Lofoten Basin which is colder by up to 3°C.

To summarize, the Nordic Seas are characterized by warm and saline inflow from the North Atlantic, and cold and fresh inflow from the Arctic Ocean. This relative hydrographic distribution is reproduced by ASTE; the eastern basins are warmer and more saline than the western basins.
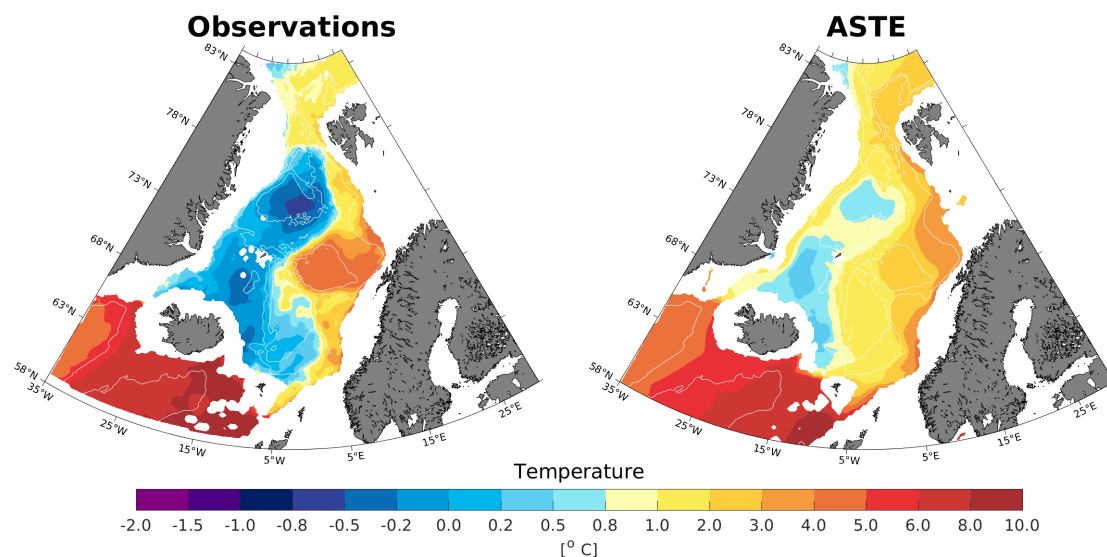
Figure 4.8: Temperature at 500 m depth, from observations (left panel) and ASTE (right panel).
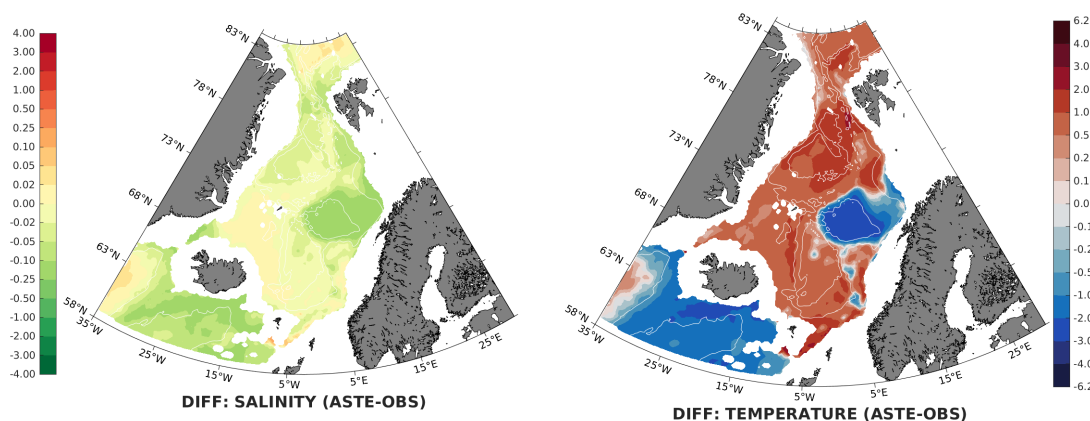

Figure 4.9: Difference between observations and ASTE in salinity (left panel) and temperature (right panel) at 500 m depth. Note the nonlinear color scale.

From the surface to 250 m, the inflowing AW is biased fresh and cold in ASTE. The Arctic Domain is too warm and fresh. ASTE overestimates the temperature in increasing areas of the Nordic Seas from the surface to 500 m depth. Below 500 m depth, the bias is reduced. Freshwater discharge into the Nordic Seas is not properly resolved, resulting in a bias towards high salinities in the EGC and Norwegian Coastal Current. From 250 m to 1000 m depth, ASTE is not able to reproduce the hydrography of the Lofoten Basin. At depth, the differences are most pronounced in the vicinity of the Lofoten Basin Eddy, which reaches down to 1200 m and has a radius of 15 - 20 km (Bosse et al., 2019). ASTE, with its nominal resolution of 16 km in the Nordic Seas, is not able to properly resolve the Lofoten Basin Eddy (Figure 4.21).

The EGC and Norwegian Coastal Current are too dense in ASTE, while the Arctic Domain is too light by approximately 0.5 kg/m^3 (Figure 4.13). The densest water is formed in the Greenland Sea, and this is also where we expect the deepest mixed layers. In general, ASTE exhibits too deep mixed layers over too large areas, particularly south of GSR where mixed-layer depths are overestimated by 1000 m (Figure 4.14). This is a common pattern in many models (Heuzé, 2021).
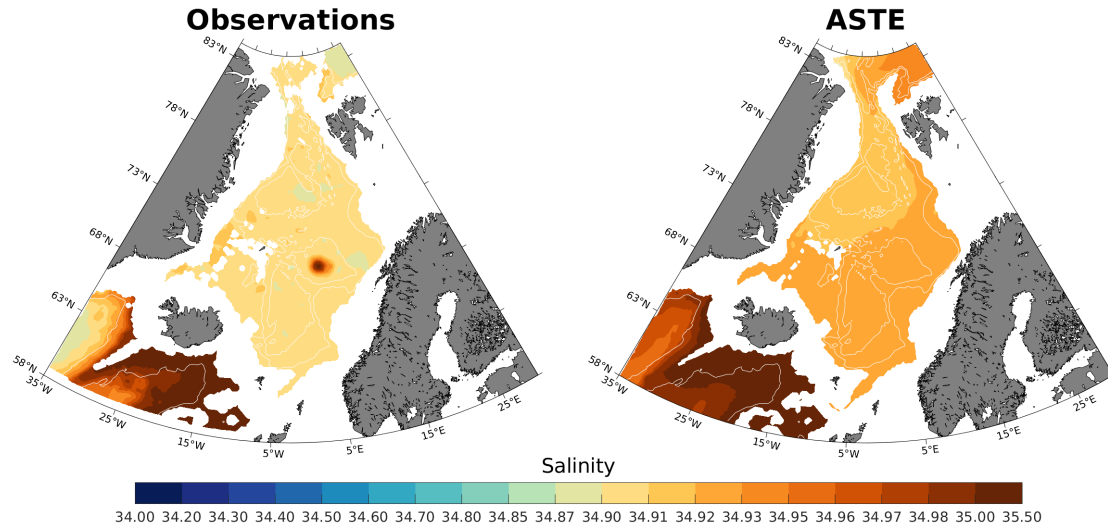
Figure 4.10: Salinity at 1000 m depth, from observations (left panel) and ASTE (right panel).
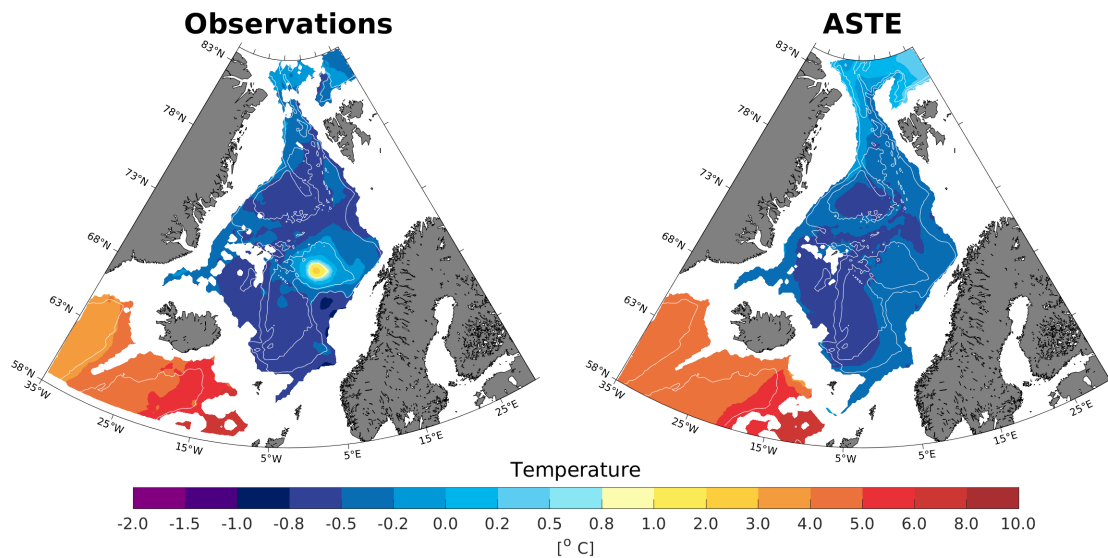

Figure 4.11: Temperature at 1000 m depth, from observations (left panel) and ASTE (right panel).

ASTE's maximum mixed-layer depths are too shallow in the Nordic Seas. This is most clearly seen in the Greenland Sea, where observed mixed layers are by far the deepest in the Nordic Seas. In the mean, the observed mixed layers reached depths of 1000 m, while mixed layers in ASTE reached only 400 m. In ASTE, the deepest mixed layers in the Nordic Seas occur in the WSC instead of in the Greenland Sea. The densest waters still occur in the Greenland Sea.

The distribution of salinity and temperature in a vertical section across the Greenland Sea and Lofoten Basin (Figure 3.1) in ASTE resembles that of the observations: The Lofoten Basin is warm and saline from the surface to 1000 m, while the Greenland Sea is cold and fresh (Figure 4.15 and 4.16). The differences between the basins are less pronounced in ASTE compared to observations, as the upper 1000 m of the Lofoten Basin are too cold and too fresh, while the upper 1000 m of the Greenland Sea are too warm and slightly too fresh (Figure 4.17). In ASTE, the $\sigma_\theta = 28.0 \ kg/m^3$ isopycnal remains flat at 600 m across the Greenland Sea, instead of doming up
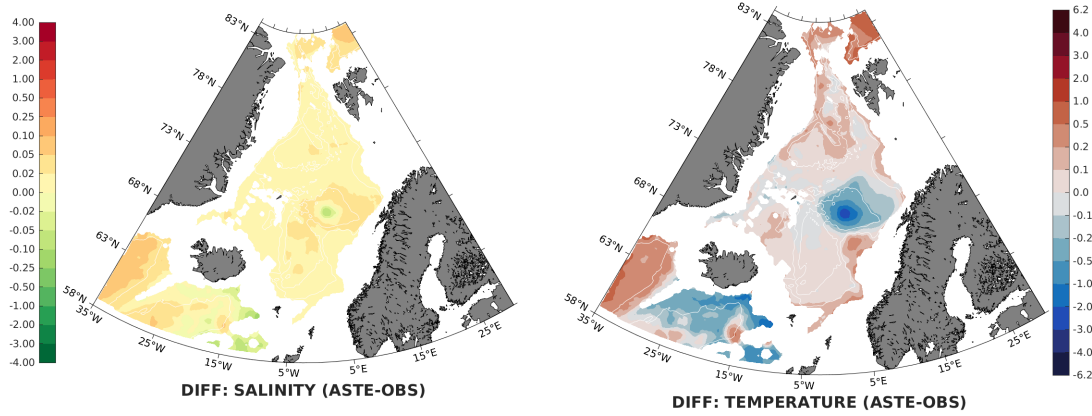
Figure 4.12: Difference between observations and ASTE in salinity (left panel) and temperature (right panel) at 1000 m depth.
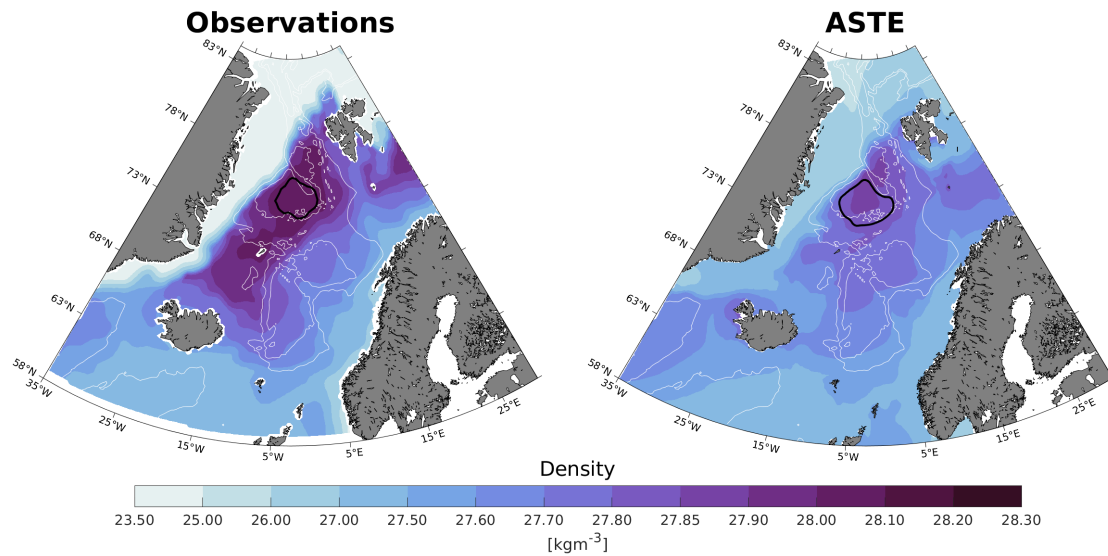
Figure 4.13: Observed (left panel) and estimated (right panel) surface density of the Nordic Seas. The black countour is the Greenland Sea Gyre.

to outcrop at the surface as in the observations. The lack of doming isopycnals in the Greenland Sea corresponds with the high bias in temperature shown in Figures 4.5 and 4.8, as the cold, intermediate waters are limited to greater depths.

The relative distributions of temperature and salinity along the crest of the GSR are largely reproduced in ASTE, yet the absolute values differ (Figures 4.18, 4.19 and 4.20). The differences result in displacements of the isopycnals, including the $\sigma_\theta = 27.8 \ kg/m^3$ isopycnal which is commonly used to delimit overflow water. We clearly see a homogenization of water mass properties in ASTE also along the GSR; cold and fresh waters are too warm and saline, while warm and saline waters are too fresh and cold. This pattern is evident through the entire Nordic Seas.
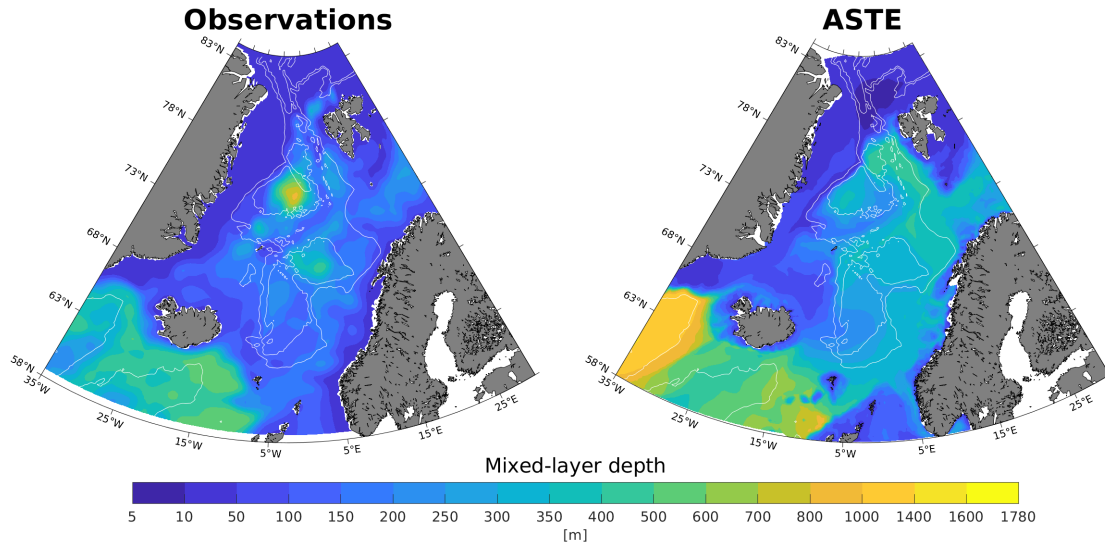
Figure 4.14: Mixed-layer depth from observations (left panel) and ASTE (right panel).

Figure 4.15: Observed (upper panel) and simulated (lower panel) salinities across the Greenland Sea and the Lofoten Basin. The white contours show potential density.

4.2 Mean circulation

The mean estimated surface velocity in the Nordic Seas in ASTE from 2002 to 2017 (all months included) is shown in the right panel of Figure 4.21. The left panel shows geostrophic velocity at the surface, calculated from satellite observations. These are averages between 2000 and 2019 (all months included). The general circulation around the boundaries of the Nordic Seas is well reproduced by ASTE. The circulation follows bathymetry to a large degree, as expected (Nost and Isachsen, 2003). The boundary circulation of the Nordic Seas, with water flowing poleward along the Norwegian coast, turning west in Fram Strait, and joining the EGC to flow back south toward GSR, is also evident in ASTE. The Norwegian Atlantic Current bifurcates into the WSC and a Barents Sea branch, and some of the WSC continues northward into the Arctic Ocean. Traces

24

Figure 4.16: Observed (upper panel) and simulated (lower panel) temperatures across the Greenland Sea and the Lofoten Basin. The white contours show potential density.

Figure 4.17: Difference between ASTE and observations in salinity (upper panel) and temperature (lower panel) across the Greenland Sea and the Lofoten Basin.

of the Lofoten Basin Eddy are evident to a depth of 1000 m (not shown), but the circulation is weaker than observed. The major difference between the observed circulation and ASTE is the missing NAFC; it is nearly non-existent as opposed to being a robust feature in the observations (e.g., Orvik and Niiler, 2002).
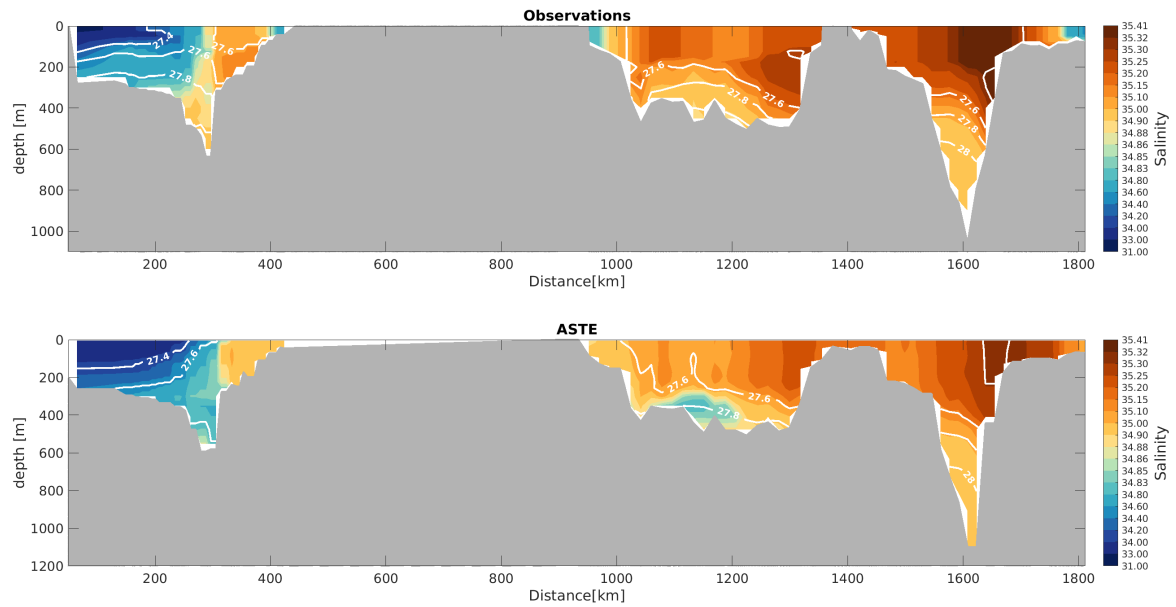
Figure 4.18: Observed (upper panel) and simulated (lower panel) salinities along the GSR. The white contours show potential density.
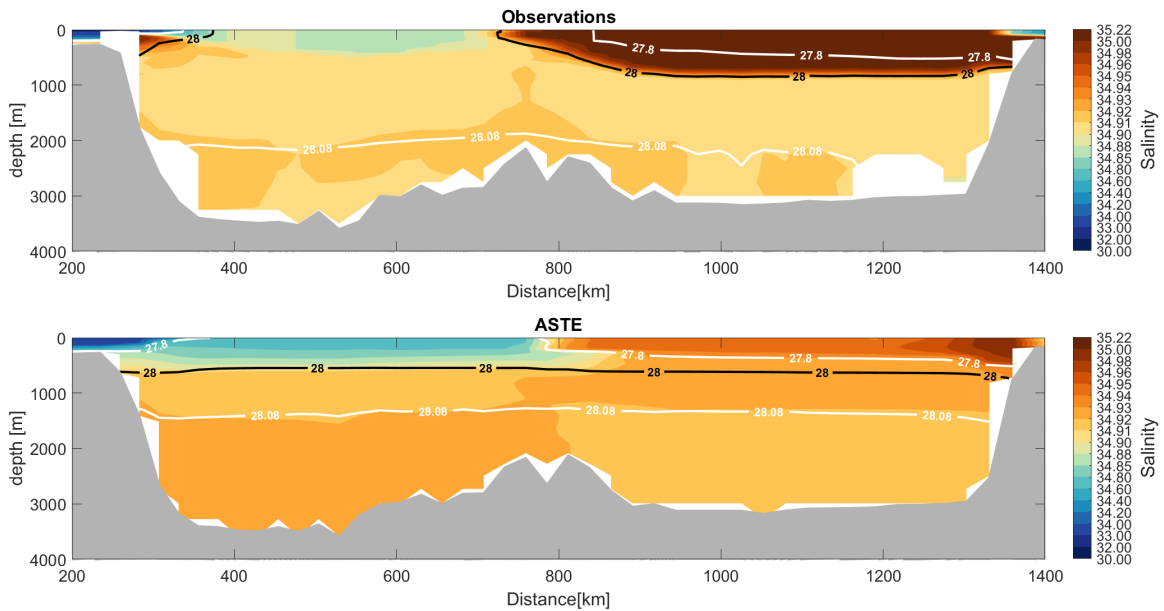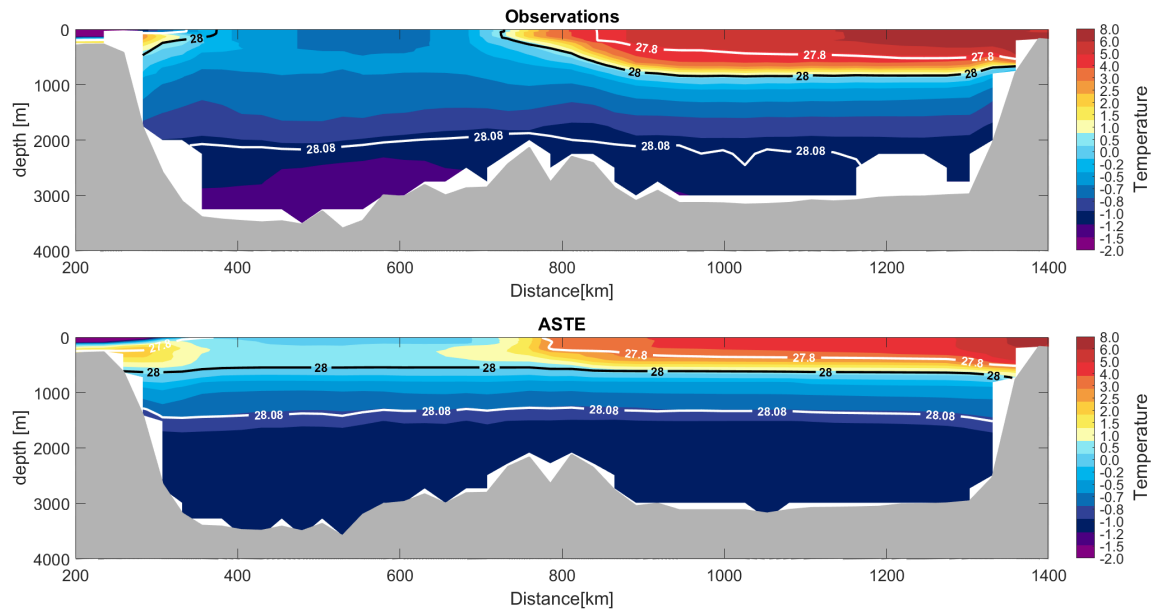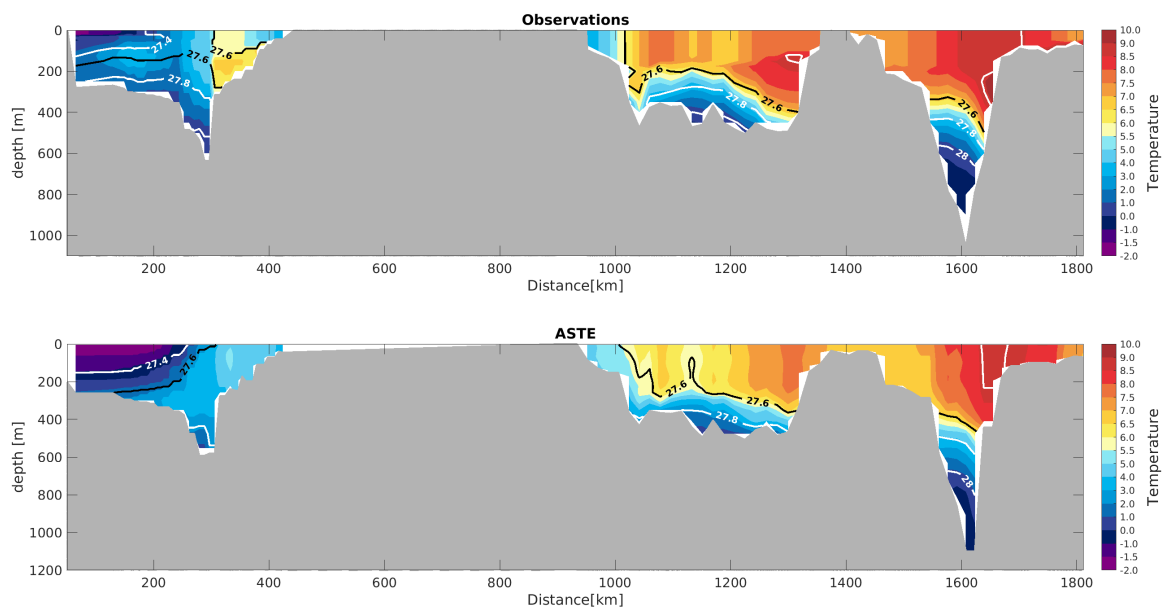

Figure 4.19: Observed (upper panel) and simulated (lower panel) temperatures along the Greenland Sea and the Lofoten Basin. The white contours show potential density.

4.3   Temporal hydrographic variability in the central Greenland Sea

Three moorings were deployed annualy in the central Greenland Sea from 1999 to 2009 (Chapter 3.2). The data from the moorings are independent from the state estimate, and overlap with the time period of ASTE from 2002 to 2009. The observed records of salinity and temperature in the central Greenland Sea from 2002 to 2009 are shown in Figures 4.22 and 4.23, along with the spatial means of salinity and temperature from the ASTE grid points enclosing the moorings. In
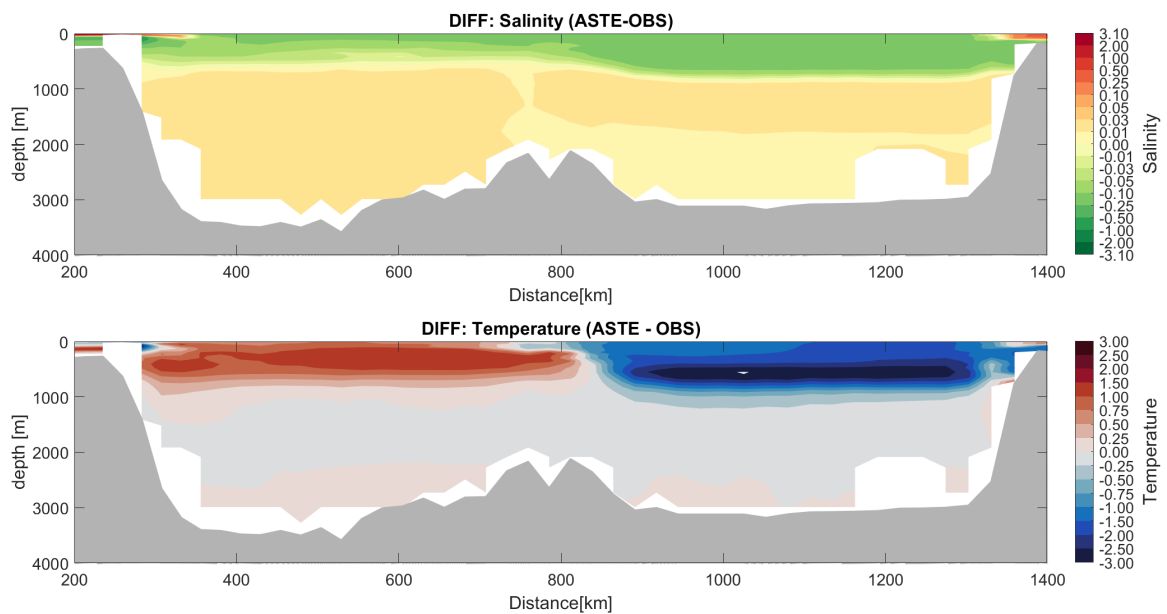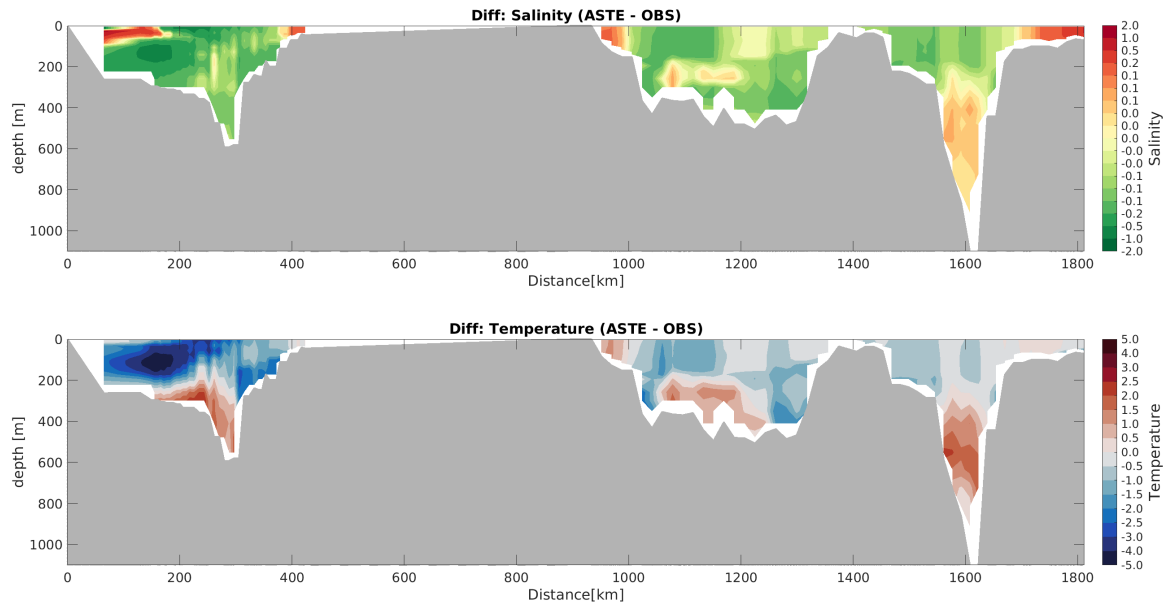
Figure 4.20: Difference between ASTE and observations in salinity (upper panel) and temperature (lower panel) along the GSR.
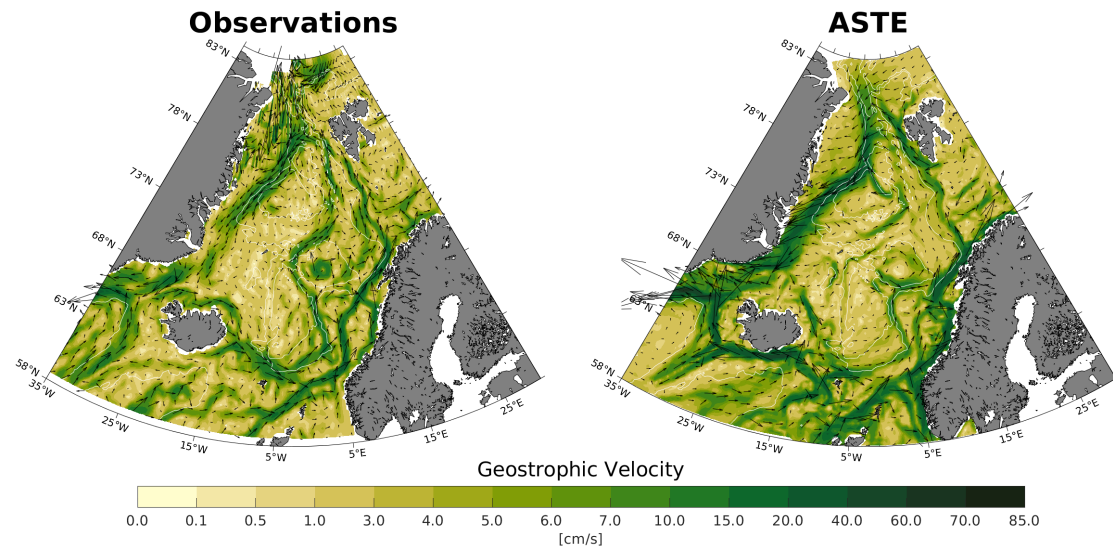
Figure 4.21: Surface velocity (black arrows) and speed (color) from satellite observations (left panel) and from ASTE (right panel). The white lines are the 500 m, 1000 m, 2000 m, and 3000 m depth contours.

ASTE, the water column was gradually getting more saline below 800 m depth throughout the period. This development is recognized also in the observations, but mostly above 1000 m, consistent with existing literature (Lauvset et al., 2018). Most of the water column was generally too saline in ASTE through the entire period, and too stratified in terms of salinity compared to the measurements. ASTE exhibited a weak salinity maximum between 1500 m and 2000 m, beneath the $\sigma_\theta = 28.08$ kg/m^3 isopycnal. A maximum in salinity was also present in the observations, but located 1000 m deeper (between 2000 m and 3000 m) in the water column. The warming of the upper 250 m in summer was overestimated in ASTE, both in intensity and depth. Down to a depth of 500 m, temperatures above zero degrees persist all year from 2002 to 2009, while in the

27

observations surface water cools to temperatures below zero degrees almost every winter.

Throughout the period, the $\sigma_\theta = 28.08 \ kg/m^3$ isopycnal remained at nearly constant depth in both the observations and the state estimate, yet it was located 500 m deeper in the observations than it was in ASTE. The $\sigma_\theta = 28.05 \ kg/m^3$ isopycnal outcropped the surface almost every winter in the observations, while remaining constant at 600 m depth in ASTE. Note that upper-ocean differences between ASTE and the observations may appear exaggerated due to the lack of observations above 100 m before 2008.

Figure 4.22: Observed (upper panel) and simulated (lower panel) temporal variability of salinity in the Greenland Sea Gyre. The white lines represent density contours.

Estimated mixed-layer depths from ASTE and mixed-layer depths identified from the observations are shown in Figure 4.24, in the central Greenland Sea between 2002 and 2009. The mixed-layer depths produced by ASTE are shallow compared to the observations; while the observed mixed-layer depths occasionally reached deeper than 1200 m, the deepest ASTE mixed layer was shallower than 600 m. The mixed-layer depths are not directly comparable, as they are determined using different routines (Chapter 3.2). To account for this, mixed-layer depths from observations where estimated using the routine by Nilsen and Falck (2006; described in Chapter 3.2) with a density difference criterion of $\Delta T = 0.8°C$, equal to that used in ASTE (not shown). The resulting mixed-layer depths were even deeper. Thus, I confidently conclude that mixed-layer depths in ASTE were much too shallow in the Greenland Sea from 2002 to 2009.
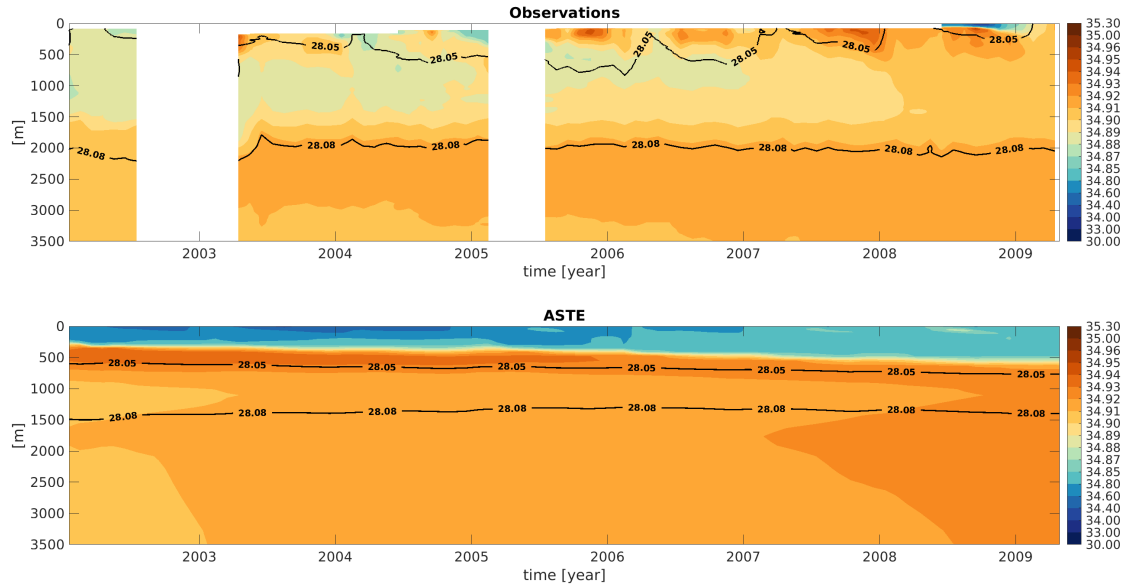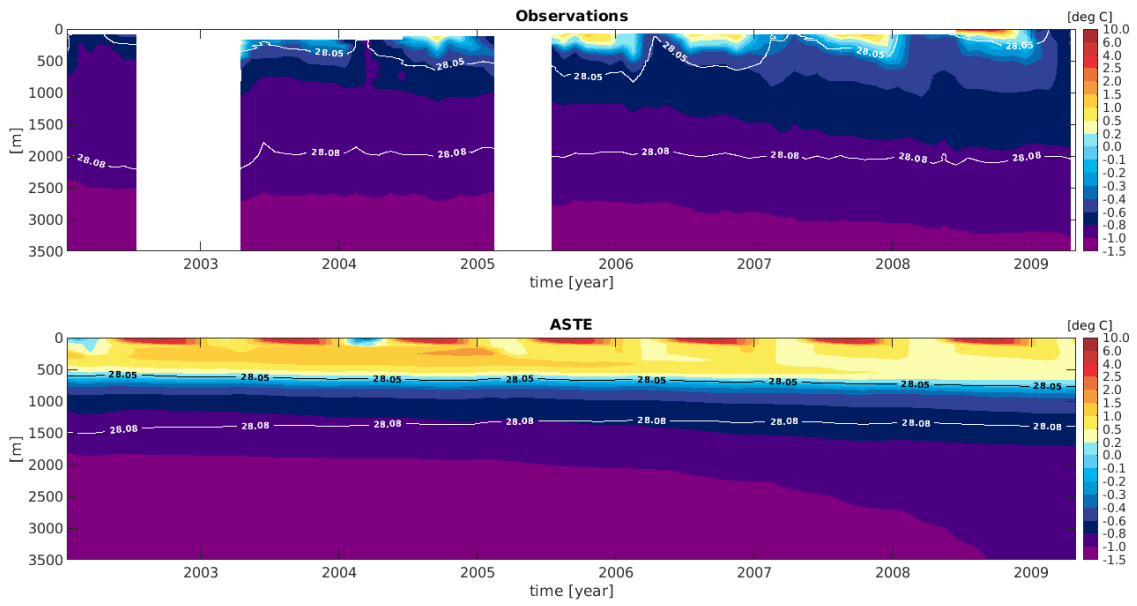
Figure 4.23: Observed (upper panel) and simulated (lower panel) temporal variability of temperature in the Greenland Sea Gyre. The white lines represent density contours.
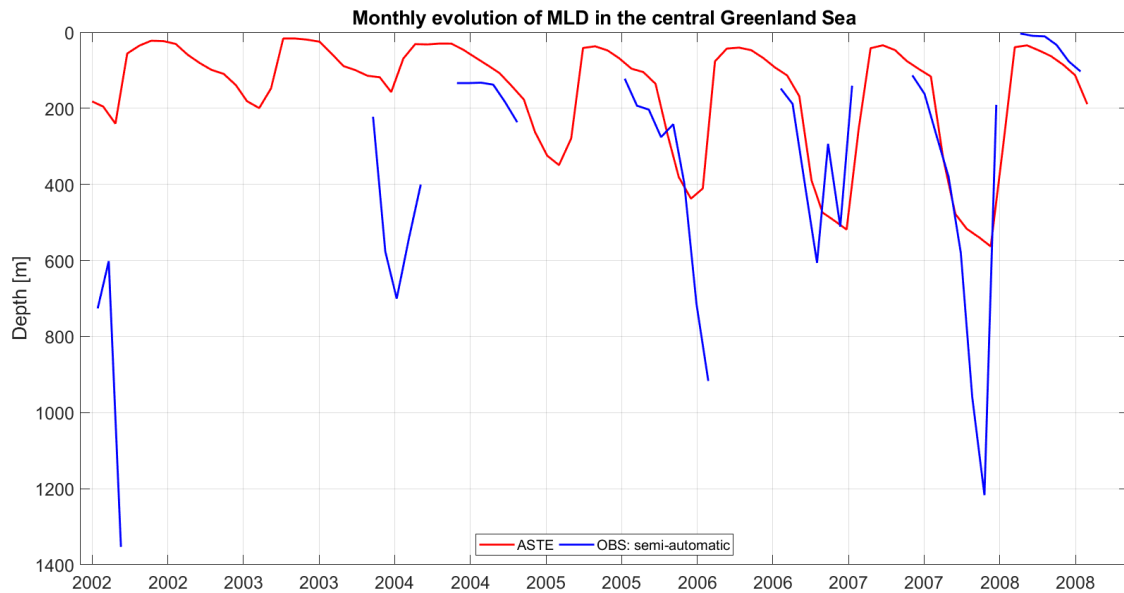
Figure 4.24: Temporal variability of mixed-layer depth in the central Greenland Sea. The blue line shows monthly mean observed mixed-layer depths. The red line shows ASTE's mixed-layer depths.

5 | Overturning in the Nordic Seas

ASTE is biased warm, fresh, and consequently light in the basins of the Nordic Seas where we expect the densest water to form. Thus, the overflow water from the Nordic Seas is too light in ASTE. This does not mean that dense water is not produced. It rather means that the usual definition of overflow water cannot be directly adopted to examine the overflow waters in ASTE. In ASTE, the overflow from the Nordic Seas across the Denmark Strait is characterized by lower limits of density ranging from 27.28 kg/m^3 to 27.81 kg/m^3 (Nguyen et al., 2021). The most including of these limits corresponds to an overflow of 1.6 ± 0.9 Sv. For comparison, Østerhus et al. (2019) estimated the dense overflow across Denmark Strait to be 3.2 ± 0.5 Sv from 1993 to 2015. Over the Iceland-Faroe Ridge, $\sigma_\theta > 27.55$ kg/m^3 yields a transport of overflow water of 0.3 ± 0.1 Sv in ASTE, compared to 0.4 ± 0.3 Sv in Østerhus et al. (2019) of water with $\sigma_\theta > 27.8$ kg/m^3. Across the Faroe-Shetland Ridge, overflow water in ASTE is characterized by a lower limit of $\sigma_\theta > 27.81$ kg/m^3. The overflow across the Faroe-Shetland Ridge is estimated to 1.8 ± 0.5 Sv in ASTE (Nguyen et al., 2021).

Only half of the observed overflow across Denmark Strait spills into the North Atlantic in ASTE, and the overflow is biased light in density. Where it originates, and which mechanisms govern its formation, are still of interest as the answer to these questions can shed light on the processes behind dense-water formation in the Nordic Seas in general. As the densest water in the Nordic Seas is formed in the Greenland Sea (Figure 4.13), I will pay particular attention the water-mass transformation there.

5.1 Water-mass transformation in the four main basins of the Nordic Seas

In this chapter I will compare the water mass properties of the Nordic Seas in *fall* (September, October, and November) to the properties of late winter (defined in the beginning of Chapter 4 as February, March and April). We expect dense-water formation in the Nordic Seas to happen primarily through formation in the interior basins of the Greenland and Iceland Seas and in the boundary-current system (Chapters 1 and 2). The change in water-mass properties from fall to late winter in all four basins of the Nordic Seas are shown in Figure 5.1. All four basins of the Nordic Seas exhibited changes from fall to late winter, especially in the form of temperature decrease (Figure 5.1). The densest water in late winter was located in the Lofoten Basin and Greenland Sea. The bulk of the water formed during winter in the Lofoten Basin was warmer and more saline than the bulk of water formed in the Greenland Sea. The late-winter properties of the Iceland Sea and Norwegian Basin were more scattered than the properties of two other basins. The properties of the Iceland Sea were mostly scattered in salinity, while the Norwegian Basin varied both in temperature and salinity. Waters of similar characteristics occupied the deep parts of all four basins.

To investigate the water-mass transformation in the Nordic Seas further, a volumetric analysis was applied as described in Chapter 3.3; through addressing densities of all grid cells in the basins to predefined density classes every month, the temporal variability of the volume constituted by each density class can be examined. All four basins exhibited seasonal variability in density throughout the year (Figures 5.2 and 5.3). A gradual densification occurred from August to April, which is when the winter-cooled water usually reached its highest densities. The densest product of wintertime cooling was found in the Greenland Sea, which reached densities between 27.84 kg/m^3 and 28.00 kg/m^3. Water in the Lofoten Basin reached densities between 27.72 kg/m^3 and 27.88 kg/m^3. The densest result of the gradual wintertime cooling in the Norwegian Basin was water of densities between 27.56 kg/m^3 and 27.72 kg/m^3, while water of densities between 27.64 kg/m^3 and 27.80 kg/m^3 dominated the Iceland Sea in late winter. For simplicity, I will refer to these four density ranges as the winter products of the Greenland Sea, the Lofoten Basin, the Norwegian Basin, and the Iceland Sea, respectively. The winter products gradually become denser from the Norwegian Basin, through the Lofoten Basin, to the Greenland Sea. This indicates a gradual cooling of AW along the boundary-current system, and further water-mass transformation in the interior Greenland Sea. Seasonal variability in even denser waters (28.04 kg/m^3 < σ_θ < 28.12 kg/m^3) occurred in all four basins, seemingly unconnected to the gradual winter transformation. If this water was ventilated in the Nordic Seas, it would be part of the gradual transformation displayed in Figure (5.3). It did not emerge from the gradual densification, and thus had to originate outside the Nordic Seas. The variability was caused by inflow from the Arctic Ocean through the western Fram Strait along the 2000 m isobath (not shown), as could be seen from the seasonal variability in horizontal distribution of these densities.
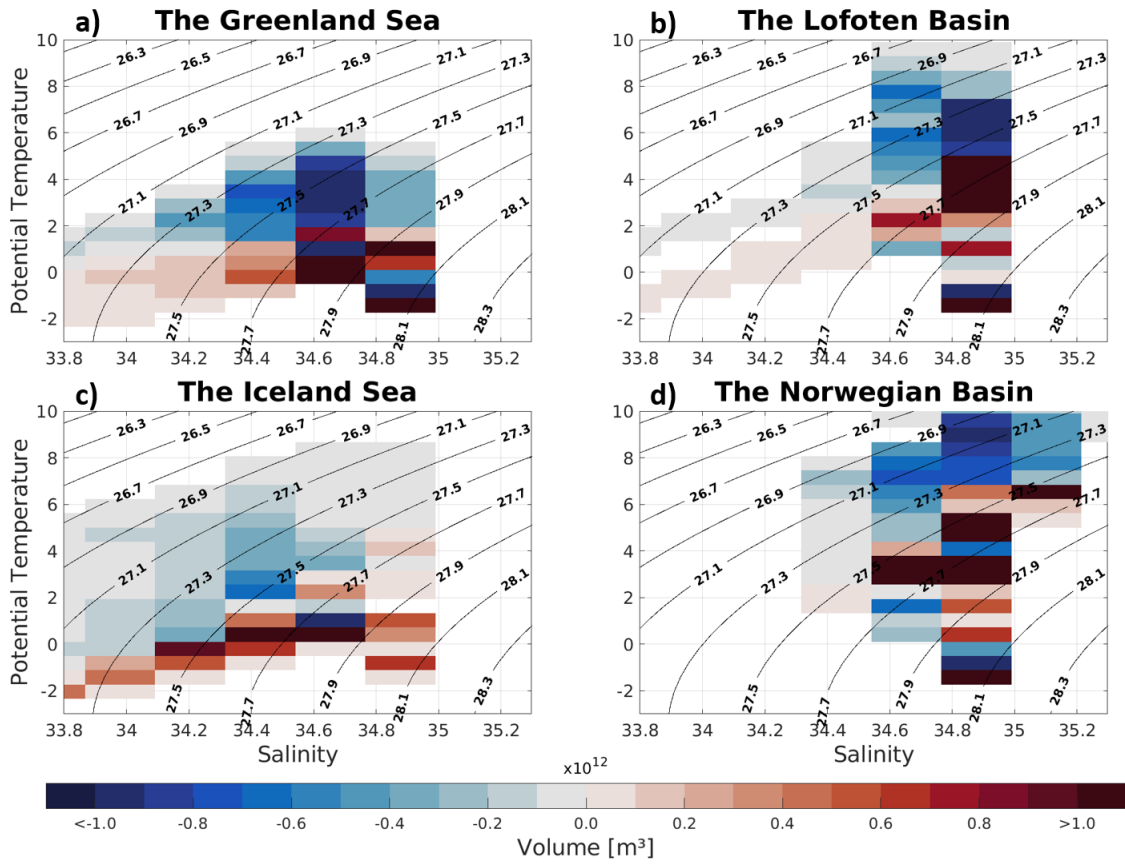
Figure 5.1: Change in hydrographic properties from fall to late winter in a) the Greenland Sea, b) the Lofoten Basin, c) the Iceland Sea and d) the Norwegian Basin. Red colors indicate that volume increased from fall to late winter, while blue colors indicate decreased volume from fall to late winter.
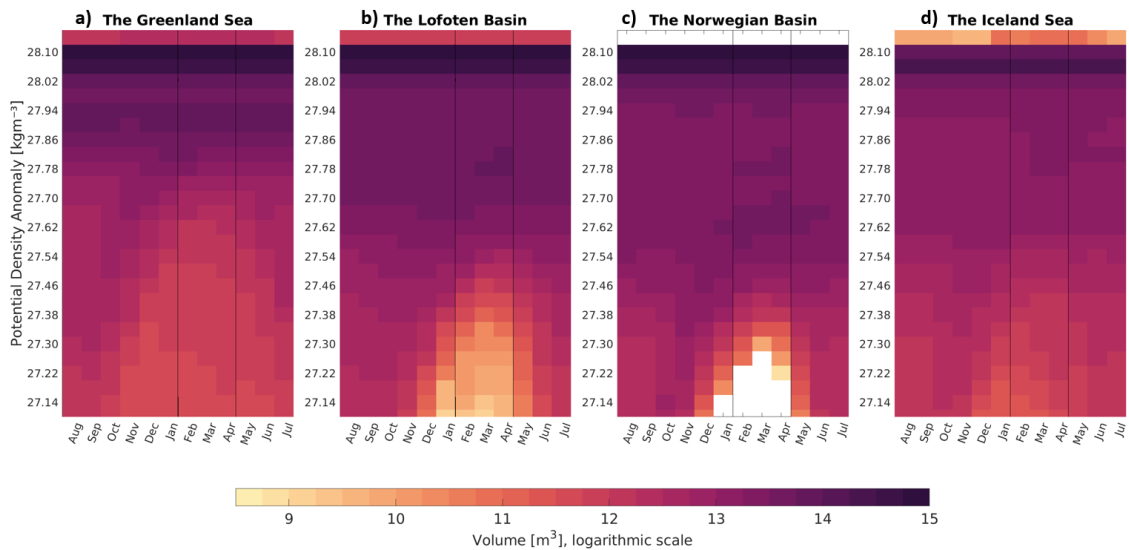
Figure 5.2: Mean monthly evolution of volume anomalies in density classes between $27.20\ kg/m^3$ and $28.14\ kg/m^3$ from August to July, in a) the Greenland Sea, b) the Lofoten Basin, c) the Norwegian Basin, and d) the Iceland Sea.
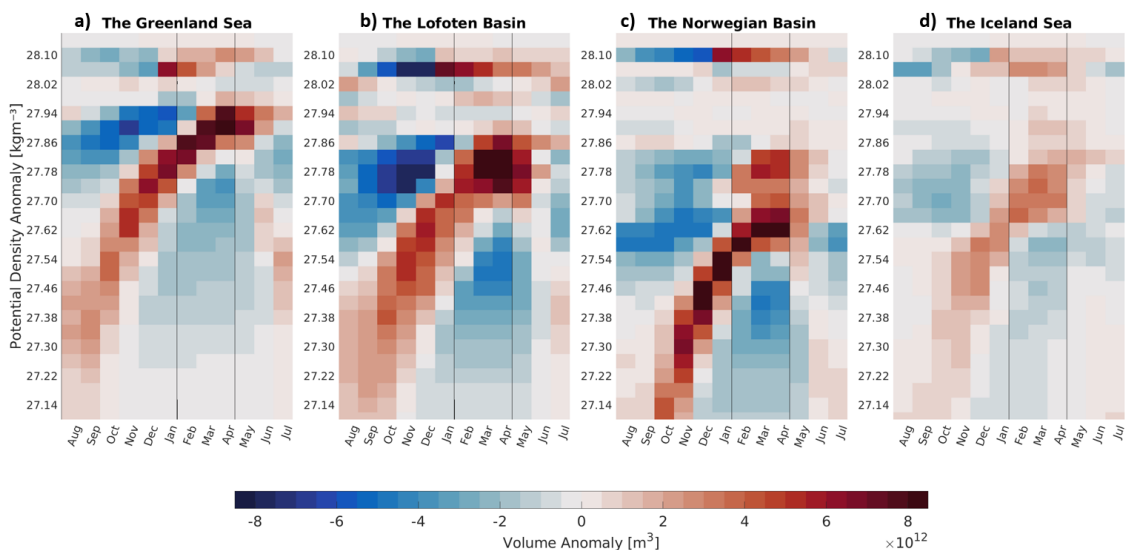
Figure 5.3: Mean monthly evolution of volume anomalies in density classes between $27.20\ kg/m^3$ and $28.14\ kg/m^3$ from August to July, in a) the Greenland Sea, b) the Lofoten Basin, c) the Norwegian Basin, and d) the Iceland Sea.

Figure 5.4: *Horizontal distribution of the winter product from the Greenland Sea:* Seasonal anomalies of depth-integrated volume of water with densities between $27.84\ kg/m^3$ and $28.00\ kg/m^3$. The anomalies are calculated with respect to the annual mean. The outer black contour outlines the Nordic Seas, and the inner black contour indicates the Greenland Sea Gyre. The yellow line is the 50% sea-ice concentration contour.

The winter product of the Greenland Sea was largely confined to that basin (Figure 5.4). This indicates local production, though inflow through Fram Strait cannot be ruled out. The highest production was located in the northern part of the basin near to Fram Strait, where highest positive volume anomalies of the winter product from the Greenland Sea were found. There is also some production of this water in the WSC, located in the Lofoten Basin. Positive volume anomalies of this winter product cross the Western Jan Mayen Ridge, and are present in the western Iceland Basin and along the Jan Mayer Ridge. These patterns indicate possible pathways of this

Figure 5.5: *Horizontal distribution of the winter product from the Lofoten:* Seasonal anomalies of depth-integrated volume of water with densities between $27.72\ kg/m^3$ and $27.88\ kg/m^3$. The anomalies are calculated with respect to the annual mean. The outer black contour outlines the Nordic Seas, and the inner black contour indicates the Greenland Sea Gyre. The yellow line is the 50% sea-ice concentration contour.
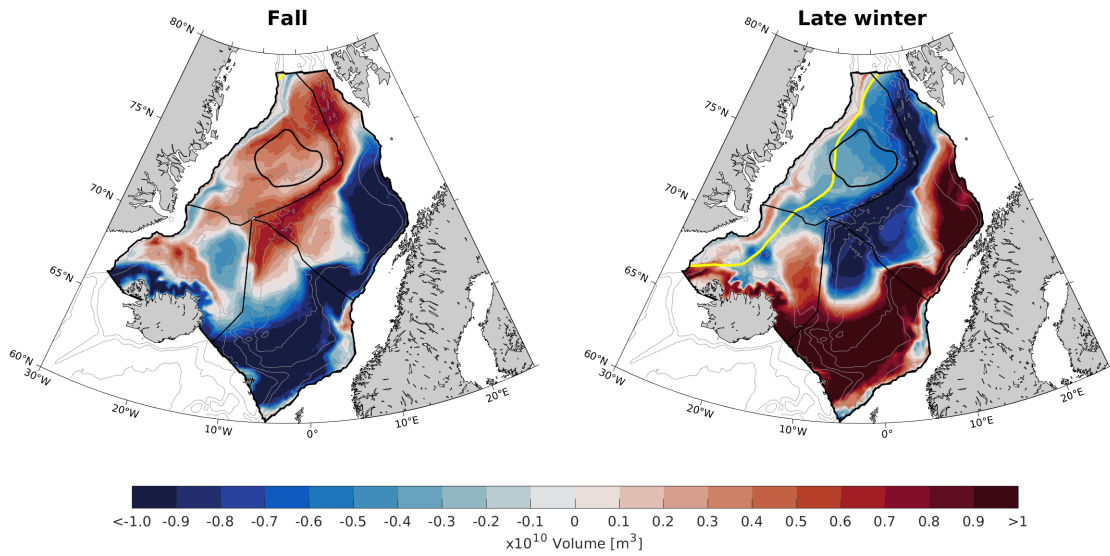
Figure 5.6: *Horizontal distribution of the winter product from the Norwegian Basin:* Seasonal anomalies of depth-integrated volume of water with densities between $27.56\ kg/m^3$ and $27.72\ kg/m^3$. The anomalies are calculated with respect to the annual mean. The outer black contour outlines the Nordic Seas, and the inner black contour indicates the Greenland Sea Gyre. The yellow line is the 50% sea-ice concentration contour.

dense water toward GSR.

The winter product of the Lofoten Basin overlapped with that of the Greenland Sea between $\sigma_\theta = 27.84\ kg/m^3$ and $\sigma_\theta = 27.88\ kg/m^3$, which can be seen in its horizontal distribution (Figure 5.5). Unlike the winter product of the Greenland Sea, the product of the Lofoten Basin was found in all four basins of the Nordic Seas. Its distribution resembled that of the NAFC rather than the NASC, as it kept west in the basin along the Mohn and Knipovich Ridges. The winter product of
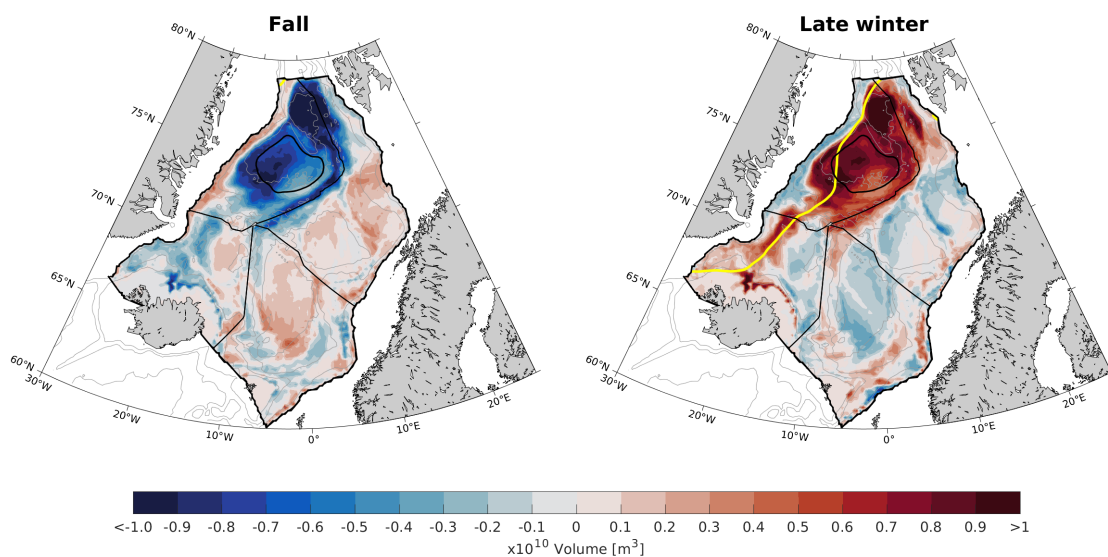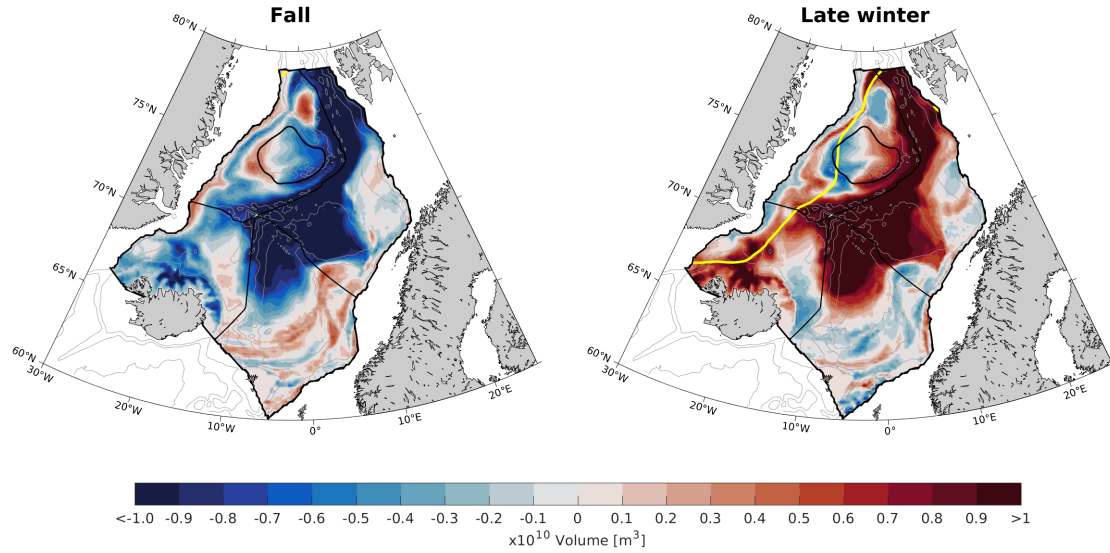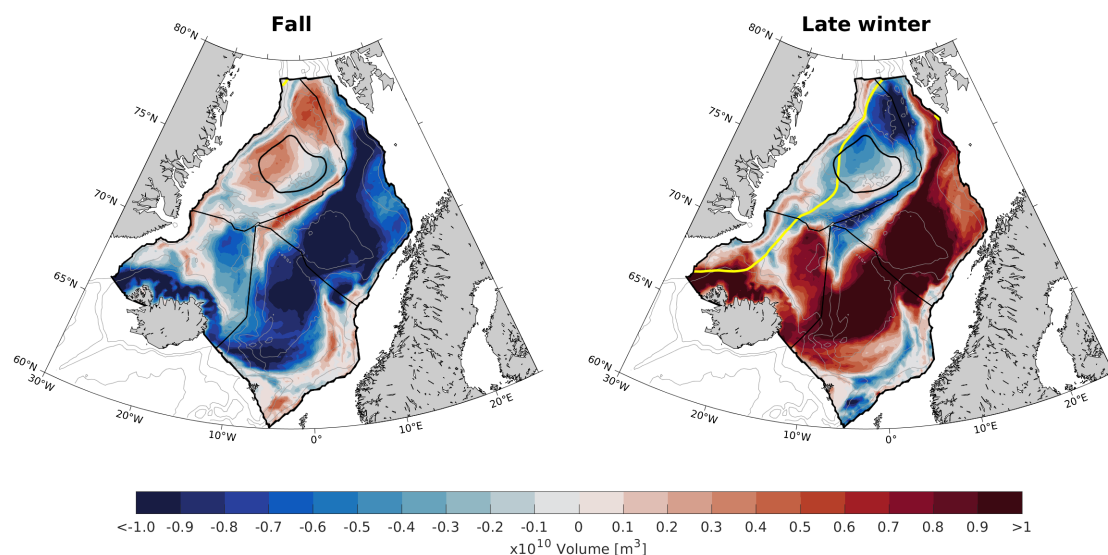
Figure 5.7: *Horizontal distribution of the winter product from the Iceland:* Seasonal anomalies of depth-integrated volume of water with densities between $27.64\ kg/m^3$ and $27.80\ kg/m^3$. The anomalies are calculated with respect to the annual mean. The outer black contour outlines the Nordic Seas, and the inner black contour indicates the Greenland Sea Gyre. The yellow line is the 50% sea-ice concentration contour.

the Norwegian Basin, on the other hand, was located along the NASC (Figure 5.6). The Iceland Sea exhibited seasonal variability in both of these winter products along the northern Iceland slope. This could be a result of local formation at the slope, or that water of these densities were transported along the shelf. The wintertime product of the Iceland Sea is distributed with large volume anomalies in the Iceland Sea, the Norwegian Sea, and the Lofoten Basin. This is not mean that water produced in the Iceland Sea occupy the Lofoten and Norwegian Basins. The winter product from the Iceland Sea has a density range in the transition between the products of the Lofoten and Norwegian Basins. It largely occupied the middle of the latter two, which is expected as the winter product of the Iceland Sea. The density, as expected, increased from south to north through the Norwegian Sea. It also increased from east to west - indicating more extensive cooling of the NAFC than of the NASC.

The average rate of dense-water production can be estimated following the method of Yashayaev and Loder (2016): by first calculating the volume of the product of interest in fall and late winter, and then dividing the difference in volume by the time between the periods. The time between fall and late winter is 5 months. The result gives us the average rate of production from fall to late winter. The mean annual production rate of the Greenland Sea winter product in the Nordic Seas was $1.0\ Sv$. The mean annual production rate of the Lofoten Basin winter product was $3.5\ Sv$ in the Nordic Seas. The winter product from the Lofoten Basin overlaps with that of the Greenland Sea, corresponding to a production rate of $0.3\ Sv$. The mean annual production rate of the winter product of the Norwegian Basin was $2.5\ Sv$. I do not consider the production rate of the Iceland Sea winter product, as it overlaps with the winter products from the Norwegian Sea and is already incorporated in the other estimated rates. Water with densities ranging from $\sigma_\theta = 27.56\ kg/m^3$ and $\sigma_\theta = 28.00\ kg/m^3$ was produced from fall to late winter on average in the Nordic Seas in ASTE. The mean annual production rate of this water was $5.5\ Sv$ in total. Note that this does not equal the sum of the individual production rates, as we have negative production of the lightest

water in the Greenland Sea. This means that water with densities equal to the winter product of the Norwegian Basin are turned into even denser water in the Greenland Sea.

5.2   Water-mass transformation in the Greenland Sea

The winter product of the Greenland Sea was distributed throughout the entire basin (Figure 5.4). From this figure alone it is unclear to what extent it was produced locally in the Greenland Sea, or if it was advected into the basin from the Arctic Ocean or the Lofoten Basin. If produced locally, it is of interest to determine whether the production is connected to the boundary-current system or to the interior basin. To investigate the production of dense water in the Greenland Sea closer, I will examine what happens inside the Greenland Sea Gyre as well.
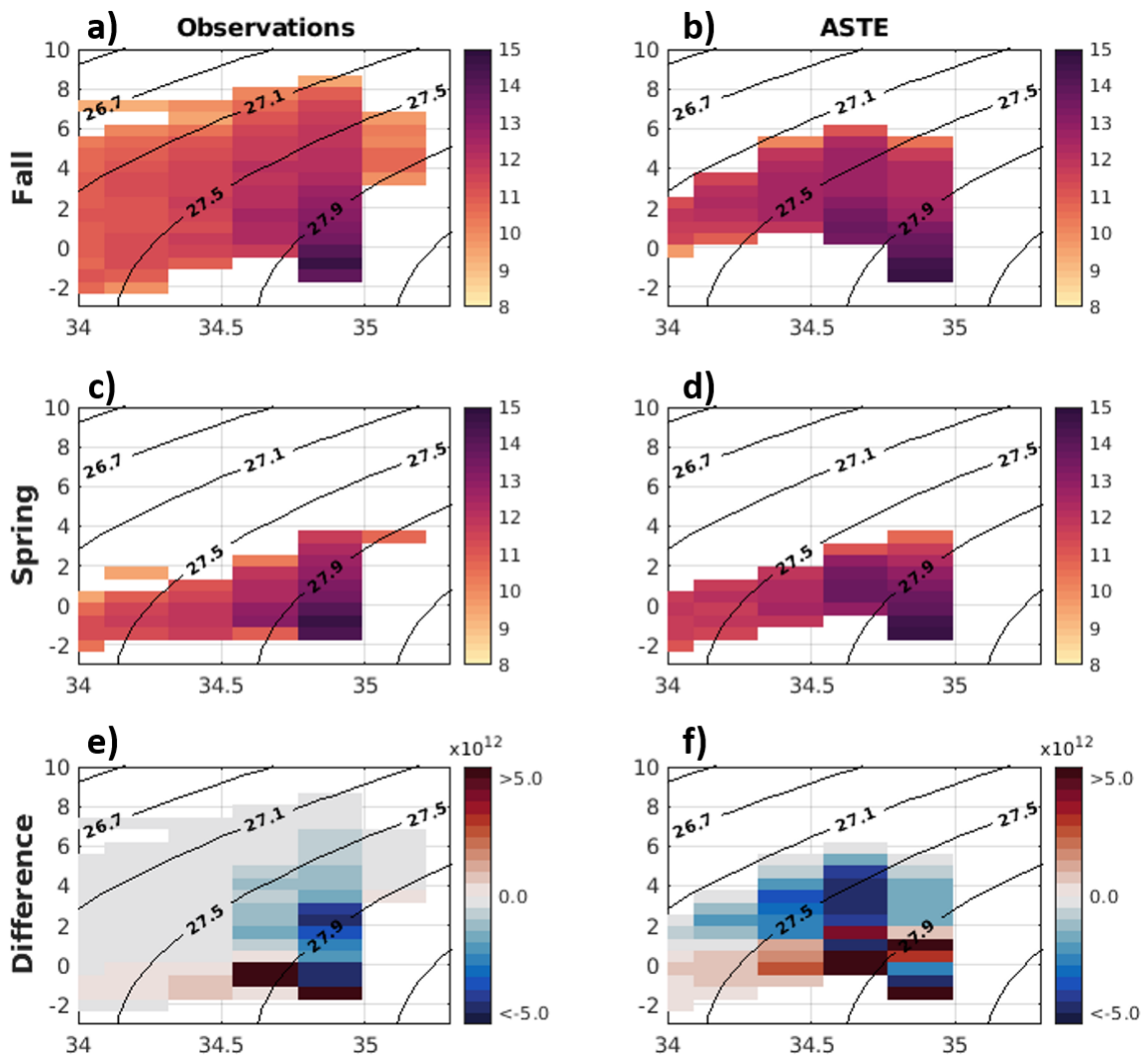
Figure 5.8: Changes in volumetric inventories from fall to late winter in the Greenland Sea from observations (left column) and ASTE (right column). The upper panels show fall values, the middle panels show late-winter values, and the lower panels show the difference from fall to late winter.

More fresh, warm water was observed in the Greenland Sea in fall than estimated in ASTE. ASTE resembled the mean late-winter properties of the Greenland Sea from 2002 to 2017 well, and

it is clear that the water mass transformation from fall to late winter happened almost exclusively through cooling (Figure 5.8). The mean dense-water production in the Greenland Sea in ASTE resulted in water with densities between $\sigma_\theta = 27.80\ kg/m^3$ and $\sigma_\theta = 28.00\ kg/m^3$ (Figure 5.9). This water was, as seen in Figures 5.4 and 5.10, distributed throughout the entire Greenland Sea, and the origin and and production cannot be determined for water in this density range as a whole. The most prominent seasonal variability inside the Greenland Sea Gyre was in densities towards the higher end of the range, between $\sigma_\theta = 27.92\ kg/m^3$ and $\sigma_\theta = 28.00\ kg/m^3$ (Figure 5.11). Water of these densities was confined exclusively to the central Greenland Sea (Figure 5.12), and hence it can be regarded a local product of the interior basin. Hereafter, I will refer to this water as the *local* winter product of the Greenland Sea. From 2002 to 2017, the mean annual production of this product was $0.3\ Sv$.

The local winter product of the water-mass transformation in the Greenland Sea was not formed throughout the entire period, but only from 2006 to 2013. To better understand which mechanisms influence its production, I investigated the covariance between the annual late-winter volume of this water mass in the central Greenland Sea in late winter and some potentially influencing variables: the late-winter net atmospheric heat flux, the late-winter sea-ice cover, the late-winter mixed-layer depth, and the preconditioning of the upper 100 m in terms of temperature and salinity in September. All correlations presented are significant within the 95% confidence interval. The volume variability was highly correlated (0.88) with the mixed-layer depth in the central Greenland Sea, another indication that the water was locally produced (Figure 5.13). It was also highly correlated (0.81) with the near-surface salinity in September, and anti-correlated (0.61) with the mean sea-ice cover. The mean net heat-loss did not significantly correlate with the volume variability. The near-surface temperature in September correlated positively (0.46) with the volume variability. The variability of sea-ice cover, net heat flux, and ocean temperature are not shown. The high correlation with surface salinity indicates that preconditioning in terms of near-surface salinity substantially influences dense-water formation in the Greenland Sea, in agreement with earlier studies (Ronski and Budéus, 2005; Latarius and Quadfasel, 2016; Brakstad et al., 2019). High surface salinity promotes convection instead of freezing by allowing the surface density to become very high as the water is cooled, and this may be the reason behind the anti-correlation between the volume variability and the amount of sea ice. A substantial sea-ice cover also isolates the ocean from the atmosphere and thus prevent high heat fluxes. It is unlikely that this is the reason for the anti-correlation between the volume evolution and sea-ice cover, as the sea ice was never close to fully covering large areas of the domain. The positive correlation with near-surface temperature in September is counter-intuitive and unexpected, as high surface temperatures increase stratification. I have not investigated the effect of wind stress on the ocean surface, another factor that may influence the mixed-layer depth by stirring the Ekman layer of the water column.
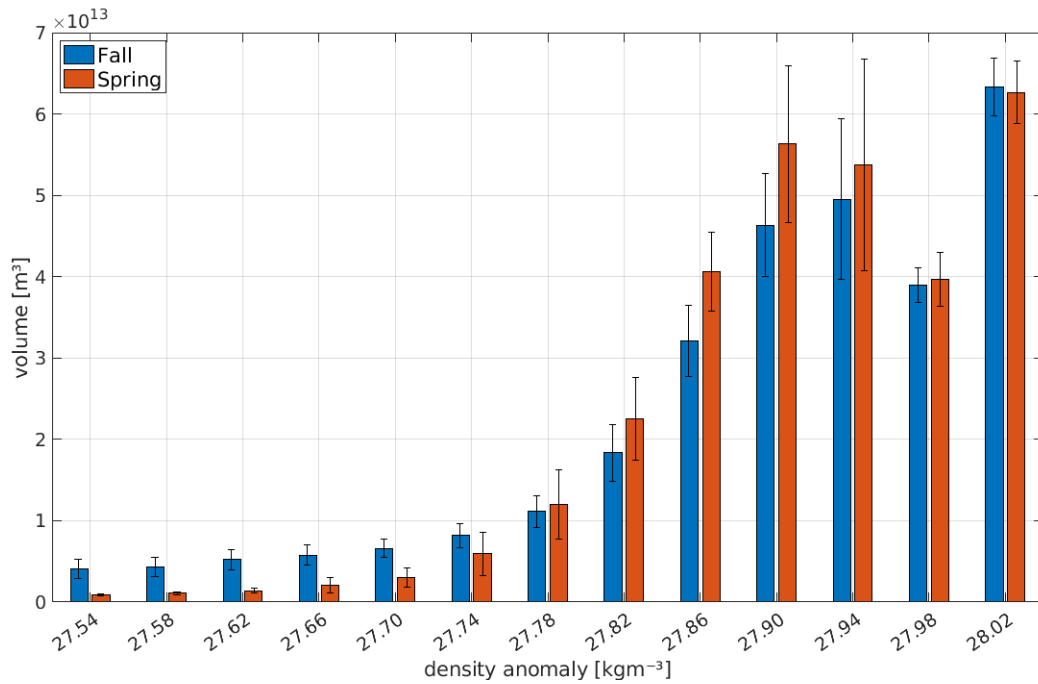
Figure 5.9: Mean volume of water in density classes ranging from $27.52 - 28.04 \ kg/m^3$ in fall (blue bars) and late winter (red bars) from 2002 to 2017 in the Greenland Sea. Error bars indicate the standard deviation.
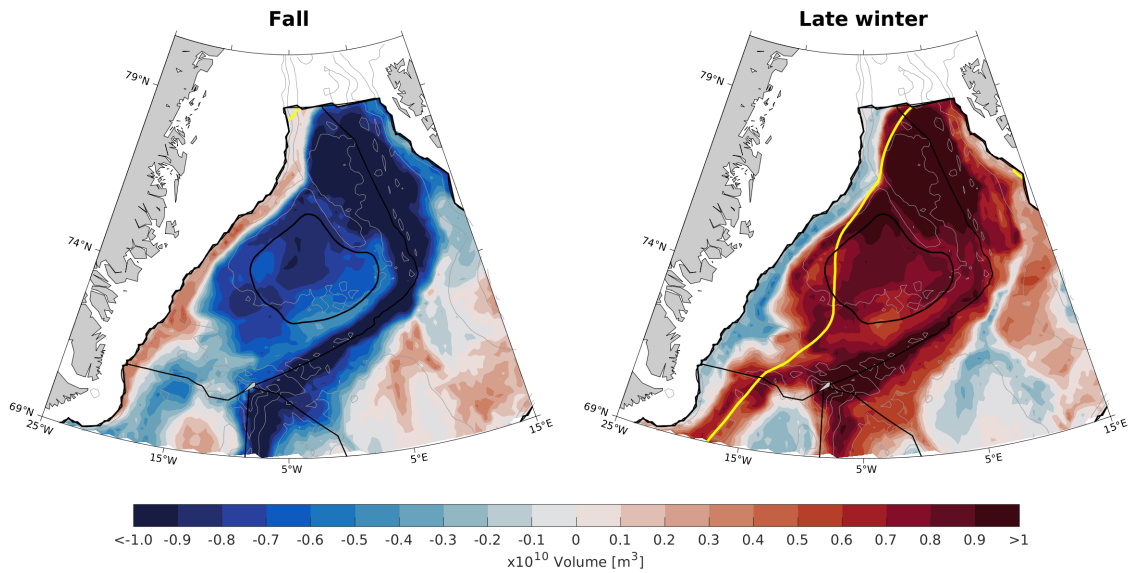
Figure 5.10: Seasonal anomalies of depth-integrated volume of water with densities between $27.80 \ kg/m^3$ and $28.00 \ kg/m^3$. The outer black contour outlines the Greenland Sea, and the inner black contour indicates the Greenland Sea Gyre. The yellow line is the 50% sea-ice concentration contour.
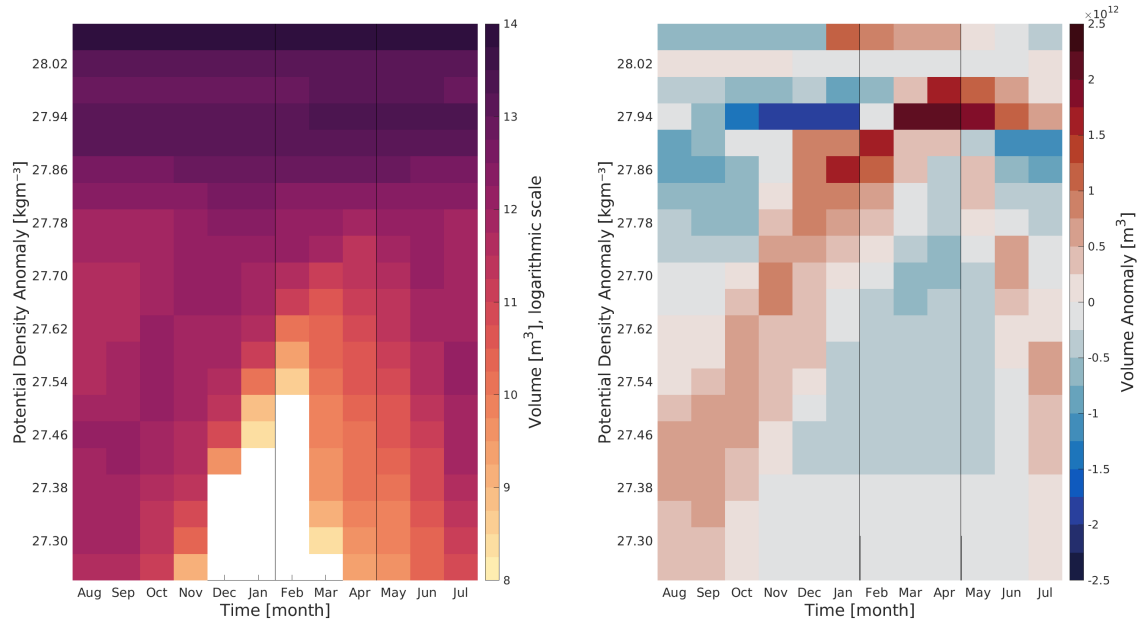
Figure 5.11: Evolution of volume occupied by water of densities between $27.10\ kg/m^3$ and $28.12\ kg/m^3$ throughout the year, averaged from 2002 to 2017. The black vertical lines mark the months February, March, and April, when we expect to find the deepest and densest mixed layers. Left panel: absolute volume (note the logarithmic color scale), left panel: volume anomalies.
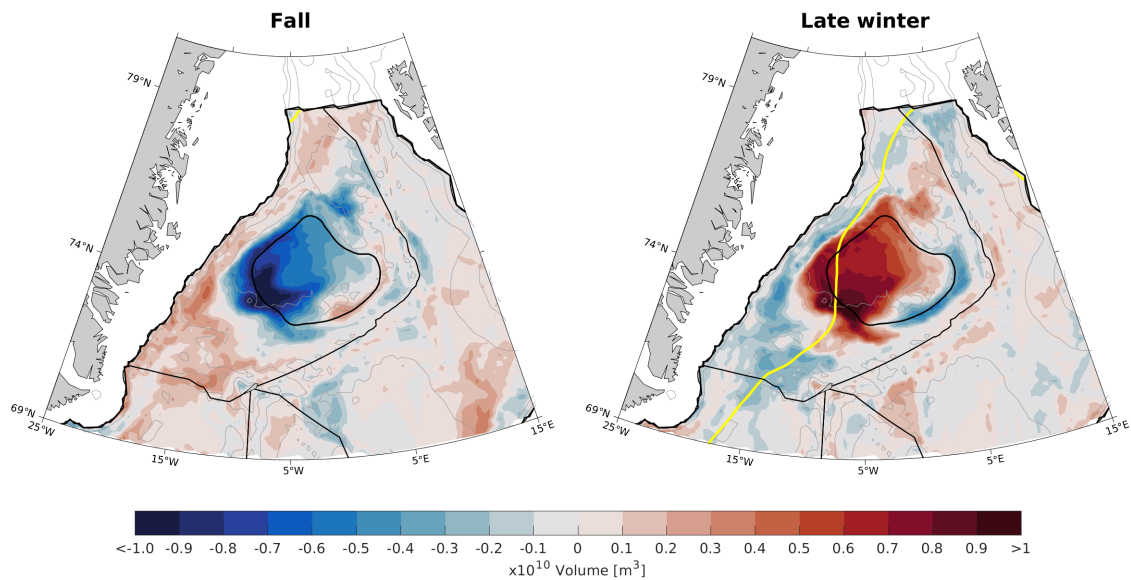
Figure 5.12: Seasonal anomalies of depth-integrated volume of water with densities between $27.92\ kg/m^3$ and $28.00\ kg/m^3$. The outer black contour outlines the Greenland Sea, and the inner black contour indicates the Greenland Sea Gyre. The yellow line is the 50% sea-ice concentration contour.
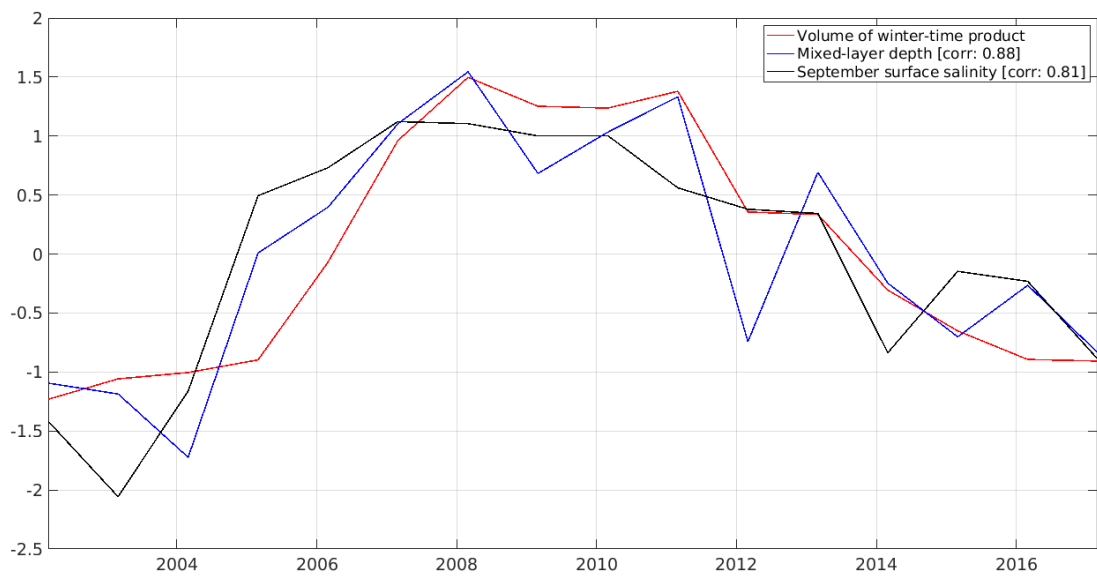
Figure 5.13: Normalized volume of the late-winter product from the Greenland Sea (black line), mixed-layer depth in late winter (blue line), and average salinity of the upper 100 m in September (black line).

6 | Discussion

In this chapter I will attempt to answer the questions stated in the introduction: How well does ASTE reproduce the main features of the Nordic Seas? How much dense water is formed in the Nordic Seas? Where is the dense water formed, and what influences the formation of dense water? First, I will discuss the limitations of the observational dataset and the challenges of comparing the state estimate to the observations. Second, I will discuss the major discrepancies between ASTE and the observations, along with their possible causes and implications. At last, I will address the overturning in the Nordic Seas from 2002 to 2017 in ASTE, and discuss to what degree it resembles that of the existing literature.

6.1   Comparing the state estimate and observations

When it comes to comparison of models and observations, some general challenges exist. Observations are often point measurements taken at a specific time, while model output represent grid-cell volumes. In ASTE, this means that a point measurement is compared to a volume with horizontal extent of 256 km^2, an area in which hydrographic characteristics may vary substantially. Having to present a continuous system in terms of discrete grid cells is a drawback of modelling, as there will always be processes too small to resolve. ASTE has a nominal resolution of 16 km in the Nordic Seas. For example, deep-convective plumes have a horizontal scale of ≤ 1 km (Marshall and Schott, 1999), and are not resolved in ASTE. Neither does ASTE resolve the Rossby radius of deformation in the Nordic Seas, and exchange of hydrographic properties by eddies are thought to be important in this area (Spall, 2010). Observational data should also be regarded with care. It is an assumption that observations, interpolated in time and space, represent the true ocean state. The hydrographic data from the Nordic Seas collected between 2000 and 2019 used to evaluate ASTE in this thesis were obtained from many sources, and have uneven temporal and spatial coverage. The Greenland shelf, for example, is undersampled compared to the rest of the domain. Thus, the late-winter observational dataset consists mostly of extrapolated values on the shelf, and one must be careful to draw conclusions about ASTE's performance there. Comparison to summer data would yield a more trustworthy evaluation of ASTE on the Greenland shelf. These are among the factors that make comparison between the state estimate and observations challenging.

6.2   How well does ASTE reproduce the features of the Nordic Seas?

The main features of the hydrography and circulation in the Nordic Seas are well reproduced in ASTE. Inflow of warm and saline AW from the North Atlantic dominates the eastern part of the

domain, and enters the Barents Sea and the Arctic Ocean farther downstream. In Fram Strait, some of it also recirculates to the south as part of the EGC. The EGC is cold and fresh, and keeps close to the East Greenland shelf break. Yet, some important features are not reproduced in ASTE. The Atlantic Domain is too cold and fresh, and the Arctic Domain is too warm and fresh. The Polar Domain is too saline. The NAFC is weak compared to observations. The NAFC emerges as a result of the strong hydrographic front between the Arctic Domain and the Atlantic Domain (Spall et al. 2010). As the inflowing AW is too cold and fresh in ASTE, while the Arctic Domain is too warm, the density difference between the domains is reduced and the front is weakened. This, in turn, results in a weakened NAFC. The characteristic weak stratification and doming isopycnals that clearly distinguishes the Arctic Domain from the Atlantic and Polar Domains are not well reproduced. Those are the very characteristics that make the Nordic Seas interesting in a global perspective, as they make the Nordic Seas one of few locations where open-ocean convection occurs.

Mixed-layer depths in the Greenland Sea are underestimated by up to 1000 m in ASTE, while overestimated in the Norwegian Sea. This may be due to the different processes of water mass transformation at the two sites; the densification of AW along the Norwegian Atlantic Current, and later in WSC, is gradual and happening over large areas. The deep convection in the Greenland Sea, on the other hand, involves abrupt convective plumes of small spatial scales ($< 1\ km$). The convective plumes cannot be directly resolved by ASTE. To look further into what could be the reason behind the underestimated mixed layers in the Greenland Sea, the factors influencing convection depth (Chapter 1 and 2) should be investigated. Locations of deep convection have some common characteristics: a weakly stratified water column beneath the seasonal pycnocline, cyclonic circulation that brings the weakly-stratified water close to the surface, a sufficiently pre-conditioned surface, and high heat fluxes to the atmosphere. In the Greenland Sea, the simulated water column beneath the pycnocline is more stratified than the observed. The resulting *convective resistance* is high, as large amounts of buoyancy needs to be removed before deep convection can occur (Frajka-Williams et al., 2014). Deep-reaching convection lowers the stratification of the water column, and thus enhances the possibility for deep-reaching convection the following year. Thus, convection depths in ASTE may be sensitive to the initial stratification of the water column. In observations, isopycnals dome upward in the Greenland Sea, exposing the weakly-stratified water more easily to the atmosphere. The gyre circulation in the Greenland Sea contributes to the doming of isopycnals; cyclonic circulation and resulting Ekman transport to the right induces divergence in the surface, which is compensated by Ekman lifting which leads to doming isopycnals. The gyre circulation in the Greenland Sea is induced by cyclonic wind stress curl and closed bathymetry contours. As isopycnals do not dome upward in ASTE, the gyre circulation must be weak. This may be due to insufficient wind forcing. The upper ocean in ASTE is too fresh in the Arctic Domain, and thus not ideally preconditioned for convection as a lot of buoyancy needs to be lost through cooling in winter before the weakly-stratified water column beneath is exposed. The mean late-winter heat flux from the ocean to the atmosphere in the Greenland Sea in ASTE was nearly constant at $100\ W/m^2$ from 2002 to 2017, which is comparable to estimates of winter turbulent heat fluxes in the area (Moore et al., 2015; Segtnan et al., 2011). Thus, I do not consider insufficient atmospheric heat loss responsible for the shallow mixed-layer depths in the Greenland Sea. Instead, I regard the high stratification of the water column, the flat isopycnals, and the low surface salinity as important factors contributing to the shallow mixed-layer depths.

6.3   How much dense water is formed in the Nordic Seas?

Overflow water is commonly defined by densities above $\sigma_\theta = 27.80 \ kg/m^3$ (e.g. Østerhus et al., 2019; Hansen and Østerhus, 2000). Because of the hydrographic biases in ASTE, however, this cannot be directly adopted when investigating overflow and dense-water formation. The overflow in Denmark Strait in ASTE varies between being denser than $\sigma_\theta = 27.28 \ kg/m^3$ and being denser than $\sigma_\theta = 27.81 \ kg/m^3$. The transport across the GSR is of course dependent on which lower density limit is used to define overflow water. The most inclusive definition of overflow water yields $1.6 \pm 0.9 \ Sv$ of overflow across Denmark Strait, while the most conservative yields an overflow of $0.5 \pm 0.3 \ Sv$ (Nguyen et al., 2021). The overflow east of Iceland also vary in characteristics, but is in closer agreement with observations. The total overflow across GSR in ASTE depends largely on the Denmark Strait overflow. Even when taking into account the biases in the Nordic Seas, the transport of overflow water across GSR from the Nordic Seas into the North Atlantic is only half of what we expect. Dependent on which definition of overflow water is applied at Denmark Strait, the total overflow across GSR in ASTE ranges from $2.6 \pm 0.9 \ Sv$ to $3.7 \pm 1.5 \ Sv$. I will refer to these numbers as the lower and upper estimate of overflow, respectively. For comparison, the observed overflow across GSR is $5.8 \pm 1.1 \ Sv$ (Østerhus et al., 2019). Realistic bathymetry is crucial for estimating transports correctly. The overflow through Denmark Strait is complex, and cannot be properly resolved with ASTE's horizontal resolution of $16 \ km$. The transport across GSR depends on the bathymetry, the velocity across the ridge and the supply of dense water. Thus, the low transports across GSR in ASTE must be caused either by insufficiently resolved bathymetry or low biases in velocity or dense-water supply.

In the following I will discuss the mean annual rates of production of dense water in the Nordic Seas that could possibly contribute to the overflow across the GSR. I consider production of waters with densities greater than, or equal to, the overflow water as possible contributions. I will start with the most including definition of overflow water, and proceed to the most conservative. Water denser than $28.00 \ kg/m^3$ was not produced in the Nordic Seas (Chapter 5.1). Therefore, I will use $\sigma_\theta = 28.00 \ kg/m^3$ as the upper limit of dense-water production in the Nordic Seas. All of the winter products from the four basins of the Nordic Seas were denser than the lowest density limit of overflow across Denmark Strait in ASTE ($\sigma_\theta = 27.28 \ kg/m^3$; Nguyen et al., 2021; Chapter 5.1). Hence, the overflow across GSR may be supplied by water from all basins of the Nordic Seas.

If we apply the lower density limit of overflow water proposed by Nguyen et al. (2021) of $\sigma_\theta = 27.28 \ kg/m^3$, the mean annual production rate of dense water was $3.3 \ Sv$ in the Nordic Seas. This is almost enough to account for the highest overflow estimate in ASTE of $3.7 \pm 1.1 \ Sv$, but not enough to supply the observed overflow across GSR of $5.8 \pm 1.5 \ Sv$ (Østerhus et al., 2019). The low production rate is partly due to negative production in the Greenland Sea, where water with densities towards the lower end of the range is turned into even denser water in winter. If we consider this the lower density limit of possible overflow water, the provision of dense water towards the GSR is too low to realistically simulate the observed overflow, and may be a main reason behind the underestimated oveflows in ASTE.

The lightest winter product of the Nordic Seas was found in the Norwegian Basin (Figure 5.3). The lower density limit of the winter product from the Norwegian Basin was $\sigma_\theta = 27.56 \ kg/m^3$, which is denser than the lowest density limit of overflow water as estimated by Nguyen et al.

(2021). When applying this as the lower density limit of potential overflow water, we get a mean annual production rate of 5.5 Sv. This is more than sufficient to account for the highest estimate of overflow in ASTE (3.7 ± 0.6 Sv; Nguyen et al., 2021), and almost enough to supply the observed overflow (5.8 ± 1.1 Sv; Østerhus et al., 2019). This production rate could almost realistically simulate the observed overflow, and indicate that the bathymetry, velocities or low densities across GSR induce the reduced overflow. The bulk (4.5 Sv) of this is production of water lighter than $\sigma_\theta = 27.80$ Sv.

When applying the conventional definition of overflow water($\sigma_\theta > 27.80$ kg/m^3), the estimated rate of annual production in the Nordic Seas was 2.1 Sv. This is nearly sufficient to supply the lowest overflow estimate in ASTE (2.7 ± 0.9 Sv), but far from enough to supply the observed transport across GSR. This definition of overflow does not take into account the biases in ASTE. Thus, it is problematic to make conclusions about dense-water formation in the Nordic Seas based on this definition of overflow water.

The Greenland Sea was the only basin where the winter product was confined to the basin's interior. Water with densities ranging between 27.92 kg/m^3 and 28.00 kg/m^3 was produced in the central Greenland Sea from 2006 to 2013 in ASTE (Chapter 5.2), and I refer to this as the local product of the Greenland Sea in ASTE. In terms of origin and production, this is comparable to the observed GSAIW, which is also a local winter product of the central Greenland Sea (Brakstad et al., 2019). The mean annual production of the local product of the Greenland Sea in ASTE was 0.3 Sv. Considering the lowest overflow estimate in ASTE across the GSR of 2.6 ± 0.6 Sv, the local production of dense water in the Greenland Sea can provide 12% of the total overflow across GSR. By comparison, the observed annual production of GSAIW from 1994 to 2014 was 0.6 ± 0.5 Sv (Brakstad et al., 2019), a rate sufficient to account for almost 10% of the total observed overflow across GSR (5.8 ± 1.1 Sv; Østerhus et al., 2019). This suggests that the Greenland Sea is nearly equally important as a provider of dense water to the GSR in ASTE as the observations indicate. The estimated production rates of GSAIW and the local product of the Greenland Sea are probably underestimated, since export from the basins is not accounted for. The horizontal volume distribution of the local product from the Greenland Sea in ASTE indicates no pathway out of the basin (Figure 5.12). Thus, the export either has to be nearly constant, or the water mixes sufficiently on its way out of the Greenland Sea that it leaves the density range displayed in Figure 5.12, and is no longer visible in the figure. As the overflow through Denmark Strait is close to constant, a constant export rate of dense water from the Greenland Sea is plausible. In the Greenland Sea, all of the water that had an average increase of volume from fall to late winter between 2002 and 2017 was denser than 27.8 kg/m^3. The total mean production of the winter product (27.84 $kg/m^3 < \sigma_\theta < 28.00$ kg/m^3) in the Greenland Sea was 1 Sv. Some of this may be locally produced, but it could also be advected into the basin from the Arctic Ocean and the Lofoten Basin. Thus, in terms of production and origin, the production rate of this water cannot be compared to the production rate of GSAIW.

The production rate of dense water in the Nordic Seas depends highly on the definitions used to delimit the potential overflow water. I argue that the lower density limit of $\sigma_\theta = 27.28$ kg/m^3 is a reasonable choice to estimate production. By utilizing this density limit, all waters transformed during winter in the Nordic Seas are included in the production rate estimate. The very densest

winter products of the Nordic Seas are too dense to cross the Denmark Strait in ASTE (Figures 4.18 and 4.19). The negative contribution from the Greenland Sea to the production estimate is thus reasonable when considering possible overflow waters. The resulting production rate of overflow water in the Nordic Seas in ASTE is 3.3 *Sv*. This is not enough to supply the observed rates of overflow across the GSR, and it is likely that the hydrographic biases in ASTE result in a reduced overflow due to insufficient supply of dense water to GSR. Production of dense water in the Nordic Seas is not necessarily entirely responsible for the reduced overflow. The overflow into the North Atlantic is a part of the AMOC, and thus connected to the other branches of the circulation. The reduced overflow from the Nordic Seas is linked to a weakened AMOC, also influenced by factors from outside the Nordic Seas (Nguyen et al., 2021).

6.4   Where are the dense water masses formed?

It is hard to determine the exact location and process of formation of dense water in the Nordic Seas based on the results in Chapter 5.1, as advection across the boundaries was not investigated. It is also not straightforward to decide on the lower density limit of overflow water, as conditions vary across the GSR. The net production rates presented in this thesis simply tell us how much the volume of a set of density classes increased from fall to late winter in ASTE in a particular domain. They do not tell us where the water is produced, how it is produced, or if it contributes to the overflow in ASTE.

Most of the fall to late-winter transformation of water denser than $\sigma_\theta = 27.80 \ kg/m^3$ occurred in the Greenland Sea (1.5 *Sv*). The Lofoten Basin produced water of these densities at an annual rate of 0.6 *Sv*. The Iceland Sea and the Norwegian Basin produced 0.2 *Sv* and 0.1 *Sv*, respectively. Hence, the Greenland Sea may supply 60% of the lowest overflow estimate in ASTE while considering densities above $\sigma_\theta = 27.80 \ kg/m^3$. Still, this water could originate outside the Greenland Sea, as it is not strictly confined to the basin (Figure 5.10)

The horizontal distributions of volume anomaly of the main wintertime products from the Lofoten and Norwegian Basins is shown in Figures 5.5 and 5.6. The product of the Norwegian Basin is lighter than that of the Lofoten Basin, and keeps further east in the domain than the denser product does. This can be explained either by more extensive cooling along the Mohn and Knipovich Ridges than along the continental slope of Norway, or by less influence from the warm waters of the Norwegian continental shelf. It could also be that influence from cold and dense water masses from the Greenland Sea and Arctic Ocean make the water in proximity to the Mohn and Knipovich Ridges denser in winter, and that the difference in density between the NAFC and NASC is partly due to distance from the Greenland Sea. The cooling of AW while progressing northward is gradual, and not confined to an enclosed area unlike convection in the Greenland Sea. Thus, a clearly defined origin of the products from these basins should not be expected.

The simulated overturning in the Nordic Seas seems to be dominated by gradually cooling AW that spreads over the entire Norwegian Sea, and convection in the central Greenland Sea. This is in good agreement with existing literature (e.g., Brakstad et al., 2019; Mauritzen,1996), as formation of dense-water both in the boundary-current system and in the interior Greenland Sea contributes to the overflow across GSR. To gain further insight into the origins of dense waters

of the Nordic Seas in ASTE, transport between the basins and across the outer boundaries of the domain must be investigated. It may also be of use to examine one density class at the time, and go deeper into the temporal variations.

6.5 Mechanisms influencing dense-water formation

Various mechanisms could potentially influence convection and formation of dense water in the Nordic Seas. Among them are the sea-ice extent, the hydrographic characteristics of the Norwegian Atlantic Current and the EGC as they enter the Nordic Seas, and the atmospheric heat fluxes. The sea-ice extent is connected to dense-water formation in two ways. The highest heat fluxes from the ocean to the atmosphere occur during cold-air outbreaks (Chapter 1), and thus the location of the ice edge influences the location of dense-water formation. On the other hand, sea ice can also inhibit the formation of dense water by insulating the ocean from the atmosphere. The salinity and temperature of the AW and EGC entering the Nordic Seas affect the convective resistance of the water column. The AW and EGC constitute the boundary current system, and thus the characteristics of these waters are directly connected to dense-water formation along the perimeter of the Nordic Seas. The salinity and temperature of the inflowing water masses also greatly influence the dense-water formation in the interior basins, as properties are exchanged between them through eddy activity. High heat fluxes to the atmosphere cause extensive cooling of the ocean, and the atmospheric heat fluxes are thus very important in formation of dense water.

Sea-ice extent, atmospheric heat fluxes, near-surface temperature and near-surface salinity were investigated in relation to the local product of the Greenland Sea (Chapter 5.2). The near-surface salinity seems to greatly influence convection depths in the central Greenland Sea in ASTE (Figure 5.13), as the two variables co-varied in time to a large extent, and had a correlation of 0.81, significant at the 95% confidence level. Earlier studies indeed show that surface salinity beneath a certain threshold can limit the effect of atmospheric cooling (Brakstad et al., 2019). As the temporal variability of sea-ice extent correlated negatively with the volume of the local winter product of the Greenland Sea, the related cold-air outbreaks seem unimportant in the formation of this water mass in ASTE. There are several possible explanations to this. Cold-air outbreaks have temporal scales on the order of 1 day (Papritz and Spengler, 2017). This analysis is based on the monthly product of ASTE, and the cold-air outbreaks may not be resolved. Since the atmospheric heat fluxes did not vary much from winter to winter (not shown), at least the strength and variability of cold-air outbreaks were not the reason behind variability in dense-water formation. Because the volume of dense water was anti-correlated with the sea-ice extent, the insulating effect of sea ice could be the dominating factor. This is unlikely, as the ice edge did not reach far into the basin any of the winters from 2002 to 2017. The negative correlation is rather a result of the common influence of near-surface salinity on sea-ice growth and convection depths; high near-surface salinity increases convection depths and inhibits sea-ice formation. Near-surface salinity is the dominating factor influencing convection depths in the Greenland Sea in ASTE. This might not have been the case if the Arctic Domain was not biased fresh. If the surface was more saline, the influences from the atmospheric heat fluxes and sea-ice extent may have been greater.

6.6 Relevance of examining overturning in the Nordic Seas in ASTE

Because of its biases, ASTE does not accurately resemble the overturning in the Nordic Seas. Too little dense water is produced, and what is produced is too light compared to observations. The resulting overflow across GSR is biased low in both density and volume, the highest overflow estimate in ASTE ($3.7 \pm 0.6\ Sv$) constitute only 64% of the observed overflow. Still, ASTE provides a means of investigating the overturning in the Nordic Seas as a whole. Because its physical consistency, changes in dense-water formation in ASTE can be traced back to its origin. Thus, ASTE should be considered a valuable tool for examining the processes influencing convection.

ASTE may be considered to represent a different climate in the Nordic Seas, where the Arctic Domain is warmer and fresher, and the AW too cold and fresh. The great salinity anomalies in the 1960s, 1980s and 1990s are evidence that such fresh conditions in the Nordic Seas are not uncommon (Belkin et al., 1998; Belkin, 2004), and knowledge about overturning in these conditions are thus of importance. More importantly, ASTE may represent the future Nordic Seas, fresher and warmer as a result of global warming. An increased hydrological cycle is expected as the climate warms (Loaiciga et al., 1996; Seager et al., 2010). An increase in the hydrological cycle includes increased precipitation, river runoff, and melting of the Greenland ice sheet. These are all factors that reduce the salinity of the Nordic Seas, and thus we should expect fresher conditions in the future. I argue that the overturning in ASTE is representative for a future climate, more than it is for the period 2002 to 2017. The overturning in the Nordic Seas in ASTE, with weak overflow and lighter waters, is a probable future outcome of global warming. The effect of the reduced overflow from the Nordic Seas to the North Atlantic across GSR is a reduction of the AMOC in ASTE (Nguyen et al., 2021), and we should consider this a possible consequence of climate change.

7 | Conclusions

The Atlantic Water in the Nordic Seas is too cold and fresh in ASTE compared to observations. The polar water in the East Greenland Current is too saline, and so is the Norwegian Coastal Current. The Greenland and Iceland Seas are too warm and fresh. The bifurcation of the Norwegian Atlantic Current into the Norwegian Atlantic Slope Current and the Norwegian Atlantic Frontal Current is not well resolved, and the latter is close to non-existent in ASTE. The hydrographic biases result in too low densities in the Greenland and Iceland Seas, and the observed deep mixed layers in the Greenland Sea are reduced by up to 1000 m in ASTE. The mixed layers in the Norwegian Sea are overestimated, especially in the West Spitsbergen Current south of Svalbard.

The formation of dense water in the Nordic Seas is dominated by gradual cooling in the boundary-current system and convection in the interior basin of the Greenland Sea. Because of the hydrographic biases, the convection in the Greenland Sea reaches 600 m at most, and the resulting dense-water formation is limited. The dense water is also biased low in density. Formation in the western part of the Norwegian Sea, in proximity to the Mohn and Knipovich Ridges, results in denser water than the formation in the eastern Norwegian Sea. Out of the four sub-basins of the Nordic Seas, the densest water in ASTE was found in the Greenland Sea ($27.84 \ kg/m^3 < \sigma_\theta < 28.00 \ kg/m^3$). The densest portion of this water ($27.92 \ kg/m^3 < \sigma_\theta < 28.00 \ kg/m^3$) is produced by convection in the Greenland Sea Gyre. The total production rate of dense water in the Nordic Seas to potentially supply the overflow across the GSR is 3.3 Sv, which is far from sufficient to account for the observed overflow of $5.8 \pm 1.1 \ Sv$. Thus it is likely that insufficient supply of dense water toward the GSR contributes to the reduced simulated overflow. In spite of the biases, the overturning in the Nordic Seas in ASTE should be considered relevant, as it represents a possible future state of overturning in a warmer climate with more freshwater in the Nordic Seas. The consequence of such fresh conditions in the Nordic Seas is reduction of the AMOC.

8 | **Outlook**

In this thesis, I have evaluated ASTE in the Nordic Seas by comparing distributions of salinity, temperature, density, velocity, and mixed-layer depths to various observations. I have also looked into the estimated overturning in the Nordic Seas. Yet, a lot more could be done to fully utilize the information that ASTE provides.

The near-surface surface salinity influences convection-depths in ASTE in the Greenland Sea to a great extent. ASTE also exhibits an increase in salinity below 800 m. An increase in the salinity of the Greenland Sea is also observed (Lauvset et al., 2018), and it is suggested that the cause of this salinification is due to increased salinity of the AW entering the Nordic Seas. Thus, it would be of great interest to examine the mechanisms influencing the salinity in the Greenland Sea, and see if the changes can be traced to the AW. The EGC acts as a source of freshwater to the Greenland Sea, while AW is the source of salt. Comparing the influence on the Greenland Sea salinity from these two sources could yield interesting information. Preliminary results show that the salinity of the upper 500 m of the Greenland Sea correlated with the diffusive salinity flux to a much greater extent than the advective flux, whereas the opposite is true at greater depths. Closed salinity and temperature budgets for the Greenland Sea could provide such information, and ASTE is an ideal tool to make such budgets.

Further investigation of the overturning in the Nordic Seas in ASTE should also be implemented. The temporal variability and spatial distribution of water in narrower density-ranges could provide more information on locations and processes of water mass transformation, information which got lost in the averaging of wide density ranges and temporal extent in this thesis. Using the NASC, NAFC, Arctic Domain and EGC as control volumes instead of the bathymetry-based volumes used in this thesis may provide more understanding of the formation processes. The exchange of water between the basins should also be investigated, as this can clarify if dense water is locally produced in a basin or advected from other basins.

In this thesis, I examined the correlation of temporal variability between volume of dense water produced, mixed-layer depth, surface salinity, net heat-fluxes, surface temperature and sea-ice coverage. These factors alone cannot explain all variability in mixed-layer depth, and other influences should be searched for. Vertical mixing due to winds could be one such candidate.

ASTE reveals inflow of dense water to the Nordic Seas from the Arctic Ocean through Fram Strait. This water could contribute to the overflow into the North Atlantic, and studies show that the AMOC may expand into the Arctic Ocean in the future. The mechanisms of overturning in the Arctic Ocean should therefore be investigated.

Bibliography

M. Årthun, T. Eldevik, and L. H. Smedsrud. The Role of Atlantic Heat Transport in Future Arctic Winter Sea Ice Loss. *Journal of Climate*, 32(11):3327–3341, jun 2019. ISSN 08948755. doi: https://doi.org/10.1175/JCLI-D-18-0750.1.

I. M. Belkin. Propagation of the "great salinity anomaly" of the 1990s around the northern north atlantic. *Geophysical Research Letters*, 31(8), 2004. doi: https://doi.org/10.1029/2003GL019334. URL `https://agupubs.onlinelibrary.wiley.com/doi/abs/10.1029/2003GL019334`.

I. M. Belkin, S. Levitus, J. Antonov, and S.-A. Malmberg. "great salinity anomalies" in the north atlantic. *Progress in Oceanography*, 41(1):1–68, 1998. ISSN 0079-6611. doi: https://doi.org/10.1016/S0079-6611(98)00015-9. URL `https://www.sciencedirect.com/science/article/pii/S0079661198000159`.

A. Brakstad, K. Våge, L. Håvik, and G. W. Moore. Water mass transformation in the Greenland sea during the period 1986-2016. *Journal of Physical Oceanography*, 49(1):121–140, 2019. ISSN 15200485. doi: 10.1175/JPO-D-17-0273.1.

A. Brakstad, K. Våge, G. Gebbie, E. Jeansson, and S. Olafsdottir. in prep.

A. Bretones, K. H. Nisancioglu, M. F. Jensen, A. Brakstad, and S. Yang. Transient Increase in Arctic Deep-Water Formation and Ocean Circulation under Sea Ice Retreat. *Journal of Climate*, 35(1):109–124, 2022. doi: 10.1175/JCLI-D-21-0152.1. URL `https://journals.ametsoc.org/view/journals/clim/35/1/JCLI-D-21-0152.1.xml`.

H. Bryden and S. Imawaki. Ocean Heat Transport. *International Geophysics*, 103:759–785, 2011. ISSN 00746142. doi: 10.1016/B978-0-12-391851-2.00029-5.

M. W. Buckley and J. Marshall. Observations, inferences, and mechanisms of the Atlantic Meridional Overturning Circulation: A review. *Reviews of Geophysics*, 54(1):5–63, 2016. doi: https://doi.org/10.1002/2015RG000493. URL `https://agupubs.onlinelibrary.wiley.com/doi/abs/10.1002/2015RG000493`.

L. Chafik and T. Rossby. Volume, Heat, and Freshwater Divergences in the Subpolar North Atlantic Suggest the Nordic Seas as Key to the State of the Meridional Overturning Circulation. *Geophysical Research Letters*, 46(9):4799–4808, 2019. ISSN 19448007. doi: 10.1029/2019GL082110. URL `https://doi.org/10.1029/2019GL082110`.

L. Chafik, H. Hátún, J. Kjellsson, K. M. H. Larsen, T. Rossby, and B. Berx. Discovery of an unrecognized pathway carrying overflow waters toward the Faroe Bank Channel. *Nature Communications*, 11(1):3721, 2020. ISSN 2041-1723. doi: 10.1038/s41467-020-17426-8. URL `https://doi.org/10.1038/s41467-020-17426-8`.

W. Cheng, J. C. H. Chiang, and D. Zhang. Atlantic Meridional Overturning Circulation (AMOC) in CMIP5 Models: RCP and Historical Simulations. *Journal of Climate*, 26(18):7187–7197, 2013. doi: 10.1175/JCLI-D-12-00496.1. URL `https://journals.ametsoc.org/view/journals/clim/26/18/jcli-d-12-00496.1.xml`.

G. Forget, J.-M. Campin, P. Heimbach, C. N. Hill, R. M. Ponte, and C. Wunsch. ECCO version 4: an integrated framework for non-linear inverse modeling and global ocean state estimation. *Geoscientific Model Development*, 8(10):3071–3104, 2015. doi: 10.5194/gmd-8-3071-2015. URL `https://gmd.copernicus.org/articles/8/3071/2015/`.

E. Frajka-Williams, P. B. Rhines, and C. C. Eriksen. Horizontal Stratification during Deep Convection in the Labrador Sea. *Journal of Physical Oceanography*, 44(1):220–228, 2014. doi: 10.1175/JPO-D-13-069.1. URL `https://journals.ametsoc.org/view/journals/phoc/44/1/jpo-d-13-069.1.xml`.

F. Fröb, A. Olsen, K. Våge, G. W. K. Moore, I. Yashayaev, E. Jeansson, and B. Rajasakaren. Irminger Sea deep convection injects oxygen and anthropogenic carbon to the ocean interior. *Nature Communications*, 7(1):13244, 2016. ISSN 2041-1723. doi: 10.1038/ncomms13244. URL `https://doi.org/10.1038/ncomms13244`.

T. Furevik, C. Mauritzen, and R. Ingvaldsen. *The flow of Atlantic water to the Nordic Seas and Arctic Ocean*, pages 123–146. Springer Berlin Heidelberg, Berlin, Heidelberg, 2007. ISBN 978-3-540-48514-8. doi: 10.1007/978-3-540-48514-8_8. URL `https://doi.org/10.1007/978-3-540-48514-8{_}8`.

B. E. Harden, R. S. Pickart, H. Valdimarsson, K. Våge, L. de Steur, C. Richards, F. Bahr, D. Torres, E. Børve, S. Jónsson, A. Macrander, S. Østerhus, L. Håvik, and T. Hattermann. Upstream sources of the Denmark Strait Overflow: Observations from a high-resolution mooring array. *Deep Sea Research Part I: Oceanographic Research Papers*, 112:94–112, 2016. ISSN 0967-0637. doi: https://doi.org/10.1016/j.dsr.2016.02.007. URL `https://www.sciencedirect.com/science/article/pii/S0967063715301266`.

B. Helland-Hansen and F. Nansen. The Norwegian Sea: its Physical Oceanography Based Upon the Norwegian Researches 1900-1904. *Report on Norwegian Fishery and Marine-Investigations*, 11(2), 1909.

C. Heuzé. Antarctic Bottom Water and North Atlantic Deep Water in CMIP6 models. *Ocean Science*, 17(1):59–90, 2021. doi: 10.5194/os-17-59-2021. URL `https://os.copernicus.org/articles/17/59/2021/`.

J. Huang, R. S. Pickart, R. X. Huang, P. Lin, A. Brakstad, and F. Xu. Sources and upstream pathways of the densest overflow water in the Nordic Seas. *Nature Communications*, 11(1):1–9, 2020. ISSN 20411723. doi: 10.1038/s41467-020-19050-y. URL `http://dx.doi.org/10.1038/s41467-020-19050-y`.

IOC, SCOR, and IAPSO. The International thermodynamic equation of seawater 2010: Calculation and use of thermodynamic properties. *Intergovermental Oceanographic Commission*, Manuals an:56, 2010.

P. E. Isachsen, C. Mauritzen, and H. Svendsen. Dense water formation in the Nordic Seas diagnosed from sea surface buoyancy fluxes. *Deep Sea Research Part I: Oceanographic Research Papers*, 54(1):22–41, 2007. ISSN 0967-0637. doi: https://doi.org/10.1016/j.dsr.2006.09.008. URL `https://www.sciencedirect.com/science/article/pii/S0967063706002573`.

M. Jakobsson, L. Mayer, B. Coakley, J. A. Dowdeswell, S. Forbes, B. Fridman, H. Hodnesdal, R. Noormets, R. Pedersen, M. Rebesco, H. W. Schenke, Y. Zarayskaya, D. Accettella, A. Armstrong, R. M. Anderson, P. Bienhoff, A. Camerlenghi, I. Church, M. Edwards, J. V. Gardner, J. K. Hall, B. Hell, O. Hestvik, Y. Kristoffersen, C. Marcussen, R. Mohammad, D. Mosher, S. V. Nghiem, M. T. Pedrosa, P. G. Travaglini, and P. Weatherall. The International Bathymetric Chart of the Arctic Ocean (IBCAO) Version 3.0. *Geophysical Research Letters*, 39(12), 2012. doi: https://doi.org/10.1029/2012GL052219. URL `https://agupubs.onlinelibrary.wiley.com/doi/abs/10.1029/2012GL052219`.

E. Jeansson, A. Olsen, and S. Jutterström. Arctic Intermediate Water in the Nordic Seas, 1991–2009. *Deep Sea Research Part I: Oceanographic Research Papers*, 128:82–97, 2017. ISSN 0967-0637. doi: https://doi.org/10.1016/j.dsr.2017.08.013. URL `https://www.sciencedirect.com/science/article/pii/S0967063716300668`.

K. Jochumsen, M. Moritz, N. Nunes, D. Quadfasel, K. M. H. Larsen, B. Hansen, H. Valdimarsson, and S. Jonsson. Revised transport estimates of the Denmark Strait overflow. *Journal of Geophysical Research: Oceans*, 122:3434–3450, 2017. ISSN 21699275. doi: 10.1002/2016JC012264.Received.

H. L. Johnson, P. Cessi, D. P. Marshall, F. Schloesser, and M. A. Spall. Recent Contributions of Theory to Our Understanding of the Atlantic Meridional Overturning Circulation. *Journal of Geophysical Research: Oceans*, 124(8):5376–5399, 2019. doi: https://doi.org/10.1029/2019JC015330. URL `https://agupubs.onlinelibrary.wiley.com/doi/abs/10.1029/2019JC015330`.

E. P. Jones, B. Rudels, and L. G. Anderson. Deep waters of the Arctic Ocean: origins and circulation. *Deep Sea Research Part I: Oceanographic Research Papers*, 42(5):737–760, 1995. ISSN 0967-0637. doi: https://doi.org/10.1016/0967-0637(95)00013-V. URL `https://www.sciencedirect.com/science/article/pii/096706379500013V`.

S. Jonsson and H. Valdimarsson. A new path for the Denmark Strait overflow water from the Iceland Sea to Denmark Strait. *Geophysical Research Letters*, 31(3):2–5, 2004. ISSN 00948276. doi: 10.1029/2003GL019214.

A. B. Kara, P. A. Rochford, and H. E. Hurlburt. An optimal definition for ocean mixed layer depth. *Journal of Geophysical Research: Oceans*, 105(C7):16803–16821, 2000. doi: https://doi.org/10.1029/2000JC900072. URL `https://agupubs.onlinelibrary.wiley.com/doi/abs/10.1029/2000JC900072`.

T. Kuhlbrodt, A. Griesel, M. Montoya, A. Levermann, M. Hofmann, and S. Rahmstorf. On the driving processes of the Atlantic meridional overturning circulation. *Reviews of Geophysics*, 45(2), 2007. ISSN 87551209. doi: 10.1029/2004RG000166.

K. Latarius and D. Quadfasel. Water mass transformation in the deep basins of the Nordic Seas: Analyses of heat and freshwater budgets. *Deep Sea Research Part I: Oceanographic Research Papers*, 114:23–42, 2016. ISSN 0967-0637. doi: https://doi.org/10.1016/j.dsr.2016.04.012. URL `https://www.sciencedirect.com/science/article/pii/S0967063716301376`.

S. K. Lauvset, A. Brakstad, K. Våge, A. Olsen, E. Jeansson, and K. A. Mork. Continued warming, salinification and oxygenation of the Greenland Sea gyre. *Tellus, Series A: Dynamic Meteorology and Oceanography*, 70(1): 1–9, 2018. ISSN 16000870. doi: 10.1080/16000870.2018.1476434. URL `https://doi.org/10.1080/16000870.2018.1476434`.

P. Lin, R. S. Pickart, K. Jochumsen, G. W. Moore, H. Valdimarsson, T. Fristedt, and L. J. Pratt. Kinematic structure and dynamics of the Denmark strait overflow from ship-based observations. *Journal of Physical Oceanography*, 50(11):3235–3251, 2020. ISSN 15200485. doi: 10.1175/JPO-D-20-0095.1.

H. A. Loaiciga, J. B. Valdes, R. Vogel, J. Garvey, and H. Schwarz. Global warming and the hydrologic cycle. *Journal of Hydrology*, 174(1):83–127, 1996. ISSN 0022-1694. doi: https://doi.org/10.1016/0022-1694(95)02753-X. URL `https://www.sciencedirect.com/science/article/pii/002216949502753X`.

K. Lorbacher, D. Dommenget, P. P. Niiler, and A. Köhl. Ocean mixed layer depth: A subsurface proxy of ocean-atmosphere variability. *Journal of Geophysical Research: Oceans*, 111(C7), 2006. doi: https://doi.org/10.1029/2003JC002157. URL `https://agupubs.onlinelibrary.wiley.com/doi/abs/10.1029/2003JC002157`.

M. S. Lozier, F. Li, S. Bacon, F. Bahr, A. S. Bower, S. A. Cunningham, M. F. De Jong, L. De Steur, B. DeYoung, J. Fischer, S. F. Gary, B. J. Greenan, N. P. Holliday, A. Houk, L. Houpert, M. E. Inall, W. E. Johns, H. L. Johnson, C. Johnson, J. Karstensen, G. Koman, I. A. Le Bras, X. Lin, N. Mackay, D. P. Marshall, H. Mercier, M. Oltmanns, R. S. Pickart, A. L. Ramsey, D. Rayner, F. Straneo, V. Thierry, D. J. Torres, R. G. Williams, C. Wilson, J. Yang, I. Yashayaev, and J. Zhao. A sea change in our view of overturning in the subpolar North Atlantic. *Science*, 363(6426):516–521, 2019. ISSN 10959203. doi: 10.1126/science.aau6592.

J. Marshall and F. Schott. Open-ocean convection; observations, theory, and models. *Reviews of Geophysics*, (37): 1–64, 1999.

J. Marshall and K. Speer. Closure of the meridional overturning circulation through Southern Ocean upwelling. *Nature Geoscience*, 5(3):171–180, 2012. ISSN 1752-0908. doi: 10.1038/ngeo1391. URL `https://doi.org/10.1038/ngeo1391`.

C. Mauritzen. Production of dense overflow waters feeding the North Atlantic across the Greenland-Scotland Ridge. Part 2: An inverse model. *Deep-Sea Research Part I: Oceanographic Research Papers*, 43(6):807–809, 1996. ISSN 09670637. doi: 10.1016/0967-0637(96)00038-6.

I. Medhaug, H. R. Langehaug, T. Eldevik, T. Furevik, and M. Bentsen. Mechanisms for decadal scale variability in a simulated Atlantic meridional overturning circulation. *Climate Dynamics*, 39:77–93, 2012. doi: 10.1007/s00382-011-1124-z. URL `https://doi.org/10.1007/s00382-011-1124-z`.

J. Meincke, S. Jonsson, and J. H. Swift. *Variability of convective conditions in the Greenland Sea.* ICES, COPENHAGEN (DENMARK), 1992. URL `https://www.proquest.com/books/variability-convective-conditions-greenland-sea/docview/16343789/se-2?accountid=8579http://openurl.bibsys.no/openurl?url{_}ver=Z39.88-2004{&}rft{_}val{_}fmt=info:ofi/fmt:kev:mtx:book{&}genre=book{&}sid=ProQ:ProQ{%}3Aasfaocean{&}atitle={&}title=Variability+of+convective+conditions+in+the+Greenland+Sea.{&}issn=0906060X{&}date=1992-01-01{&}volume={&}issue={&}spage=32{&}au=Meincke{%}2C+J{%}3BJonsson{%}2C+S{%}3BSwift{%}2C+J+H{&}isbn={&}jtitle={&}btitle=Variability+of+convective+conditions+in+the+Greenland+Sea.{&}rft{_}id=info:eric/2850236{&}rft{_}id=info:doi/`.

M. B. Menary, D. L. R. Hodson, H. I. Robinson, and R. A. Sutton, R. T.and Wood. A Mechanism of Internal Decadal Atlantic Ocean Variability in a High-Resolution Coupled Climate Model. *Jorunal of Climate*, 28(19): 7764–7785, 2015. doi: 10.1175/JCLI-D-15-0106.1. URL `https://doi.org/10.1175/JCLI-D-15-0106.1`.

G. W. Moore, K. Vage, R. S. Pickart, and I. A. Renfrew. Decreasing intensity of open-ocean convection in the Greenland and Iceland seas. *Nature Climate Change*, 5(9):877–882, 2015. ISSN 17586798. doi: 10.1038/nclimate2688.

A. T. Nguyen, D. Menemenlis, and R. Kwok. Arctic ice-ocean simulation with optimized model parameters: Approach and assessment. *Journal of Geophysical Research: Oceans*, 116(C4), 2011. doi: https://doi.org/10.1029/2010JC006573. URL https://agupubs.onlinelibrary.wiley.com/doi/abs/10.1029/2010JC006573.

A. T. Nguyen, H. Pillar, V. Ocaña, A. Bigdeli, T. A. Smith, and P. Heimbach. The Arctic Subpolar Gyre sTate Estimate: Description and Assessment of a Data-Constrained, Dynamically Consistent Ocean-Sea Ice Estimate for 2002–2017. *Journal of Advances in Modeling Earth Systems*, 13(5):e2020MS002398, 2021. doi: https://doi.org/10.1029/2020MS002398. URL https://agupubs.onlinelibrary.wiley.com/doi/abs/10.1029/2020MS002398.

K. W. Nicholls, S. Østerhus, K. Makinson, T. Gammelsrød, and E. Fahrbach. Ice-ocean processes over the continental shelf of the southern Weddell Sea, Antarctica: A review. *Reviews of Geophysics*, 47(3), 2009. doi: https://doi.org/10.1029/2007RG000250. URL https://agupubs.onlinelibrary.wiley.com/doi/abs/10.1029/2007RG000250.

J. E. Nilsen and E. Falck. Variations of mixed layer properties in the Norwegian Sea for the period 1948–1999. *Progress In Oceanography*, 70:58–90, 2006. doi: 10.1016/j.pocean.2006.03.014.

O. Nost and P. Isachsen. The large-scale time-mean ocean circulation in the Nordic Seas and Arctic Ocean estimated from simplified dynamics. *Journal of Marine Research*, 61, 2003. doi: 10.1357/002224003322005069.

K. A. Orvik and P. Niiler. Major pathways of Atlantic water in the northern North Atlantic and Nordic Seas toward Arctic. *Geophysical Research Letters*, 29(19):2–4, 2002. doi: https://doi.org/10.1029/2002GL015002. URL https://agupubs.onlinelibrary.wiley.com/doi/abs/10.1029/2002GL015002.

S. Østerhus, R. Woodgate, H. Valdimarsson, B. Turrell, L. de Steur, D. Quadfasel, S. M. Olsen, M. Moritz, C. M. Lee, K. M. H. Larsen, S. Jónsson, C. Johnson, K. Jochumsen, B. Hansen, B. Curry, S. Cunningham, and B. Berx. Arctic Mediterranean exchanges: a consistent volume budget and trends in transports from two decades of observations. *Ocean Science*, 15(2):379–399, 2019. doi: 10.5194/os-15-379-2019. URL https://os.copernicus.org/articles/15/379/2019/.

L. Papritz and T. Spengler. A Lagrangian Climatology of Wintertime Cold Air Outbreaks in the Irminger and Nordic Seas and Their Role in Shaping Air–Sea Heat Fluxes. *Journal of Climate*, 30(8):2717–2737, 2017. doi: 10.1175/JCLI-D-16-0605.1. URL https://journals.ametsoc.org/view/journals/clim/30/8/jcli-d-16-0605.1.xml.

T. Petit, M. S. Lozier, S. A. Josey, and S. A. Cunningham. Atlantic Deep Water Formation Occurs Primarily in the Iceland Basin and Irminger Sea by Local Buoyancy Forcing. *Geophysical Research Letters*, 47(22):1–9, 2020. ISSN 19448007. doi: 10.1029/2020GL091028.

R. S. Pickart, D. J. Torres, and R. A. Clarke. Hydrography of the labrador sea during active convection. *Journal of Physical Oceanography*, 32(2):428 – 457, 2002. doi: 10.1175/1520-0485(2002)032<0428:HOTLSD>2.0.CO;2. URL https://journals.ametsoc.org/view/journals/phoc/32/2/1520-0485_2002_032_0428_hotlsd_2.0.co_2.xml.

P. Rhines, S. Häkkinen, and S. A. Josey. Is oceanic heat transfer significant in the climate system? In B. Dickson, J. Meincke, and P. Rhines, editors, *Arctic-Subarctic Ocean Fluxes: Defining the Role of the Northern Seas in Climate*, chapter 6, pages 87–109. 2008.

S. Ronski and G. Budéus. Time series of winter convection in the Greenland Sea. *Journal of Geophysical Research C: Oceans*, 110(4):1–11, 2005. ISSN 01480227. doi: 10.1029/2004JC002318.

R. Seager, N. Naik, and G. A. Vecchi. Thermodynamic and dynamic mechanisms for large-scale changes in the hydrological cycle in response to global warming. *Journal of Climate*, 23(17):4651 – 4668, 2010. doi: 10.1175/2010JCLI3655.1. URL https://journals.ametsoc.org/view/journals/clim/23/17/2010jcli3655.1.xml.

O. H. Segtnan, T. Furevik, and A. D. Jenkins. Heat and freshwater budgets of the Nordic seas computed from atmospheric reanalysis and ocean observations. *Journal of Geophysical Research: Oceans*, 116(C11), 2011. doi: https://doi.org/10.1029/2011JC006939. URL https://agupubs.onlinelibrary.wiley.com/doi/abs/10.1029/2011JC006939.

S. Semper, K. Våge, R. S. Pickart, H. Valdimarsson, D. J. Torres, and S. Jónsson. The Emergence of the North Icelandic Jet and Its Evolution from Northeast Iceland to Denmark Strait. *Journal of Physical Oceanography*, 49 (10):2499–2521, 2019. doi: 10.1175/JPO-D-19-0088.1. URL `https://journals.ametsoc.org/view/journals/phoc/49/10/jpo-d-19-0088.1.xml`.

S. Semper, R. S. Pickart, K. Våge, K. M. H. Larsen, H. Hátún, and B. Hansen. The Iceland-Faroe Slope Jet: a conduit for dense water toward the Faroe Bank Channel overflow. *Nature Communications*, 11(1):1–10, 2020. ISSN 20411723. doi: 10.1038/s41467-020-19049-5. URL `http://dx.doi.org/10.1038/s41467-020-19049-5`.

D. A. Smeed, S. A. Josey, C. Beaulieu, W. E. Johns, B. I. Moat, E. Frajka-Williams, D. Rayner, C. S. Meinen, M. O. Baringer, H. L. Bryden, and G. D. McCarthy. The North Atlantic Ocean Is in a State of Reduced Overturning. *Geophysical Research Letters*, 45(3):1527–1533, 2018. ISSN 19448007. doi: 10.1002/2017GL076350.

W. H. F. Smith and D. T. Sandwell. Global Sea Floor Topography from Satellite Altimetry and Ship Depth Soundings. *Science*, 277(5334):1956–1962, may 1997. ISSN 00368075, 10959203. URL `http://www.jstor.org/stable/2893884`.

M. A. Spall. Non-local topographic influences on deep convection: An idealized model for the Nordic Seas. *Ocean Modelling*, 32(1):72–85, 2010. ISSN 1463-5003. doi: https://doi.org/10.1016/j.ocemod.2009.10.009. URL `https://www.sciencedirect.com/science/article/pii/S1463500309002054`.

V. H. Strass, E. Fahrbach, U. Schauer, and L. Sellmann. Formation of denmark strait overflow water by mixing in the east greenland current. *Journal of Geophysical Research: Oceans*, 98(C4):6907–6919, 1993. doi: https://doi.org/10.1029/92JC02732. URL `https://agupubs.onlinelibrary.wiley.com/doi/abs/10.1029/92JC02732`.

K. Svingen, A. Brakstad, K. Våge, W. Jon von Appen, and L. Papritz. The effect of cold air outbreaks and lateral heat fluxes on dense-water formation in the Greenland Sea from a ten-year moored record (1999-2009). *Journal of Physical Oceanography*, in prep.

J. H. Swift and K. Aagaard. Seasonal transitions and water mass formation in the Iceland and Greenland seas. *Deep Sea Research Part A, Oceanographic Research Papers*, 28(10):1107–1129, 1981. ISSN 01980149. doi: 10.1016/0198-0149(81)90050-9.

J. H. Swift, K. Aagaard, and S.-A. Malmberg. The contribution of the Denmark strait overflow to the deep North Atlantic. *Deep Sea Research Part A. Oceanographic Research Papers*, 27(1):29–42, 1980. ISSN 0198-0149. doi: https://doi.org/10.1016/0198-0149(80)90070-9. URL `https://www.sciencedirect.com/science/article/pii/0198014980900709`.

T. Tsubouchi, K. Våge, B. Hansen, K. Larsen, S. Østerhus, C. Johnson, S. Jonsson, and H. Valdimarsson. Increased ocean heat transport into the Nordic Seas and Arctic Ocean over the period 1993–2016. *Nature Climate Change*, 11:1–6, 2021. doi: 10.1038/s41558-020-00941-3.

K. Våge, R. S. Pickart, M. A. Spall, H. Valdimarsson, S. Jónsson, D. J. Torres, S. Østerhus, and T. Eldevik. Significant role of the North Icelandic Jet in the formation of Denmark Strait overflow water. *Nature Geoscience*, 4(10):723–727, 2011. ISSN 1752-0908. doi: 10.1038/ngeo1234. URL `https://doi.org/10.1038/ngeo1234`.

K. Våge, G. W. K. Moore, S. Jónsson, and H. Valdimarsson. Water mass transformation in the Iceland Sea. *Deep Sea Research Part I: Oceanographic Research Papers*, 101:98–109, 2015. ISSN 0967-0637. doi: https://doi.org/10.1016/j.dsr.2015.04.001. URL `https://www.sciencedirect.com/science/article/pii/S0967063715000680`.

I. Yashayaev and J. W. Loder. Recurrent replenishment of labrador sea water and associated decadal-scale variability. *Journal of Geophysical Research: Oceans*, 121(11):8095–8114, 2016. doi: https://doi.org/10.1002/2016JC012046. URL `https://agupubs.onlinelibrary.wiley.com/doi/abs/10.1002/2016JC012046`.